Size Effects on Surface Chemistry and Raman Spectra of Sub-5 nm Oxidized HPHT and Detonation Nanodiamonds

Stepan Stehlik, Michel Mermoux, Bernhard Schummer, Ondrej Vanek, Katerina Kolarova, Pavla Stenclova, Ales Vlk, Martin Ledinsky, Rene Pfeifer, Oleksandr Romanyuk, et al.

Size Effects on Surface Chemistry and Raman Spectra of sub-5 nm Oxidized HPHT and Detonation Nanodiamonds

Stepan Stehlik[1], Michel Mermoux[2], Bernhard Schummer[3], Ondrej Vanek[4], Katerina Kolarova[1], Pavla Stenclova[1], Ales Vlk[1], Martin Ledinsky[1], Rene Pfeifer[1], Oleksandr Romanyuk[1], Ivan Gordeev[1], Francine Roussel-Dherbey[5], Zuzana Nemeckova[6], Jiri Henych[6,7], Petr Bezdicka[6], Alexander Kromka[1], Bohuslav Rezek[8]*

[1] Institute of Physics of the Czech Academy of Sciences, Cukrovarnická 10, 162 00 Prague 6, Czechia

[2] Univ. Grenoble Alpes, Univ. Savoie Mont Blanc, CNRS, Grenoble INP, LEPMI, 38000 Grenoble, France

[3] Würzburg University, Chair for X-Ray Microscopy, Josef-Martin-Weg 63, 97074 Würzburg, Germany

[4] Department of Biochemistry, Faculty of Science, Charles University, Hlavova 2030/8, 128 40, Prague, Czechia

[5] Univ. Grenoble Alpes, Grenoble INP, CMTC, 38000 Grenoble, France

[6] Institute of Inorganic Chemistry of the Czech Academy of Sciences, 250 68 Husinec-Řež, Czechia

[7] J.E. Purkyně University in Ústí nad Labem, Králova výšina 7,400 96 Ústí nad Labem, Czechia

[8] Faculty of Electrical Engineering, Czech Technical University in Prague, Technická 2, 166 27, Prague, Czechia

KEYWORDS: detonation nanodiamond, HPHT nanodiamond, particle size distribution, surface chemistry, Raman spectroscopy, phonon confinement, breathing modes

ABSTRACT

Understanding materials with dimensions down to few nanometers is of major importance for fundamental science as well as prospective applications. Structural transformation and phonon-confinement effects in the nanodiamonds (NDs) have been theoretically predicted below 3 nm size. Here we investigate the effect of size on the surface chemistry, microscopic structure, and Raman scattering of high-pressure high-temperature (HPHT) and detonation nanodiamonds (DNDs) down to 2-3 nm. The surface and size of NDs are controlled by annealing in air and ultracentrifugation resulting in three ND fractions. Particle size distribution (PSD) of the fractions is analyzed by combining dynamic light scattering (DLS), analytical ultracentrifugation (AUC), small angle X-ray scattering (SAXS), X-ray diffraction (XRD), and transmission electron microscopy (TEM) as complementary techniques. Based on the obtained PSD we identify size-dependent and synthesis-dependent differences of NDs properties. In particular, interpretation of Raman scattering on NDs is revisited. Comprehensive comparison of detonation

and pure monocrystalline HPHT NDs reveals effects of diamond core size and defects, chemical and temperature (in)stability as well as limitations of current phonon confinement models. In addition, low-frequency Raman scattering in the 20 – 200 cm^{-1} range is experimentally observed. The size dependence of this signal for both HPHT NDs and DNDs suggests that it may correspond to confined acoustic vibrational, "breathing-like" modes of NDs.

Introduction

Diamond nanoparticles, so called nanodiamonds (NDs), represent a class of carbon-based nanomaterials in which the carbon atoms in the nanoparticle core have mostly sp^3 hybridization as in the bulk diamond. This provides NDs several unique properties such as high chemical inertness, extreme hardness as well as the possibility to host various active color centers including the most studied nitrogen-vacancy (NV) or silicon-vacancy (SiV) [1–3]. The NDs surface also enables broad surface chemistry modifications including specialized and complex functionalities [4–6]. The surface chemistry of NDs can be readily adjusted by thermal or plasma treatments and the nature of surface atoms (e.g. hydrogen or oxygen or even sp^2 carbon) can be used to control colloidal and optoelectronic properties such as zeta potential, work function or photoluminescence [7–10].

Nowadays, two most common types of NDs are produced by a controlled detonation of explosives or by a high-pressure high-temperature (HPHT) synthesis. While the detonation nanodiamonds (DNDs) are characterized by a rather narrow size distribution of their primary nanoparticles with a mean size around 5±2 nm, the HPHT NDs have typically broader size distributions as a result of the grinding process they arise from. Yet, the finest commercial HPHT

ND powders contain dominant number of sub-10 nm NDs [11] which can be isolated by centrifugation of ND colloids [12].

The availability of diamond nanoparticles with a mean particle size lower than 10 nm and produced by different preparation routes offers interesting opportunities, both from technological and fundamental scientific viewpoints. In particular, obtaining HPHT NDs with a controlled size distribution, surface chemistry, particle core with excellent crystallinity and active optical centers [13] can be beneficial. However, there is no broadly accepted standard among NDs [14]. Therefore, some of the characteristics of these nanoparticles are still a matter of debate. Comparison of NDs of different origin on similar size scale down to several nanometers could bring some new insights and answers to some of currently open questions. For example, what is the effect of size on the ND structure down to several nanometers in terms of crystallinity, non-diamond carbon content, and surface chemistry?

Among various methods so far used for ND characterization, Raman spectroscopy is usually considered as a method of choice for the analysis of such nanoparticles, see for example Ref. [15] and references therein. Recently, this technique, as well as TEM imaging, indeed revealed significant differences in the crystallinity of these two ND types at a similar size scale [12]. Moreover, Raman spectroscopy has been widely used to extract a size distribution of NDs by modeling the diamond Raman line shape parameters (shift, width and asymmetry) [8,15–22] according to the so-called phonon confinement model. However, for the lowest size distributions, in the 1-10 nm range, the DNDs have been almost exclusively modeled ignoring the various structural defects that do contribute to the line shape. Indeed, recent advances in preparation of ultra-small DNDs (2-3 nm) indicated that the diamond Raman line shape of DND is rather insensitive to size changes [23,24], i.e. the diamond Raman line shape of DND is

predominantly given by the poor crystallinity and not by the ~ 5 nm size. However, monocrystalline HPHT NDs, having the size as the only parameter influencing the Raman line shape, are on the ultra-small size scale still missing.

In this study, we report the method used to extract both HPHT and DND nanoparticles with size distributions well below 10 nm with, a volumetric mode down to around 3 nm, and with a very low sp^2-C content. We show that characterizing the particle size distribution (PSD) of sub-10 nm ND by only a single technique might be problematic and in some cases may lead to even misleading results. Therefore, we combine several different methods, correlate their outputs, and discuss relation between the methods and samples. Size dependent surface chemistry and structure of NDs are then characterized by several spectroscopic techniques, with emphasis on the use of Raman spectroscopy. In particular, the availability of the monocrystalline sub-5 nm ND with a narrow size distribution provides an opportunity to re-interpret the diamond Raman spectrum at the nanoscale and to point out strong differences between the two types of NDs. Pure monocrystalline sub-10 nm HPHT NDs are used to elucidate the effects of size and structure on the Raman spectra of NDs in general. We discuss some possible limitations of the current phonon confinement models usually used to extract a mean particle size from the diamond Raman line profiles. We also investigate the low-frequency Raman scattering which seems to contain some information about the NDs size as well.

Experimental

Samples preparation

As monocrystalline HPHT NDs we used MSY 0-0.03 powder (Microdiamant; purity: 99.5%) with a median size of 18 nm and size distribution in the 0-30 nm range. This ND powder

is, to our knowledge, one of the finest commercial HPHT ND powder available currently on the market. It arises from the grinding of HPHT-synthesized diamond monocrystals, resulting in monocrystalline NDs with superior crystallinity but intrinsic broad size distribution. As such, monocrystalline HPHT NDs are suitable for the investigation of size-related effects, e.g. confinement effects, since possible shifts and broadening of the diamond Raman peaks can be related solely to the size effect with minimal contribution of lattice defects. It has been shown that similar MSY 0-0.05 ND powder (median size 25 nm) contain a dominant number of sub-10 nm NDs, whose volume/mass is, however, less than 3 wt.% [11]. The as-received HPHT ND powder was processed as follows. At first 400 mg was annealed under ambient atmosphere at 450 °C for 5 hours in order to suppress sp^2 carbon content [12]. Weight loss during the annealing was 20%. After this treatment, the NDs became oxidized and are thus further denoted as HPHT O-NDs. The preparation of size-reduced DNDs has already been described in [23]. Briefly, 400 mg of the as-received DND powder (New Metals and Chemicals Corp.; purity: > 98%) with a nominal size of 5 nm was annealed under ambient atmosphere at 520 °C for 50 minutes (weight loss 80%) in order to reduce the average size of the DND particles. This sample is further denoted as size-reduced oxidized DNDs (SR O-DNDs).

Three different size fractions of both HPHT O-ND and SR O-DND samples were obtained using the following protocol: 20 mg of ND powder was dispersed in 2 mL of DI water and sonicated for one hour using a Hielscher UP 200s sonicator and S2 sonotrode. The obtained colloidal solutions were centrifuged in two subsequent centrifugation steps starting with 2 mL of ND colloid using a centrifuge (Eppendorf minispin plus). The two centrifugation steps at 14,000 rpm (13,124 g) lasted 1.5 h. After the first centrifugation step 1 mL (i.e. half of the tube content) of the supernatant was taken by a micropipette for the second centrifugation step (using 2 mL of

the first supernatant) at the same conditions. After the second step the final 1 mL of the supernatant was taken. Such prepared double-centrifuged fractions are further labeled as "c1". Next, 2 mL of the c1 fraction was used for further fractionation by means of a table top ultracentrifuge (Optima Max XP, Beckman Coulter) using a swinging bucket TLS-55 rotor. Two ultracentrifugation runs of 2 mL of the c1 fractions were performed at 55,000 rpm (259,000 × g) and lasted either 1 hour or 3 hours, after which 1 mL of supernatant were carefully extracted, resulting in two fractions further labeled as "uc2" and "uc3", respectively. Commercial single-digit DND (denoted as SD-DND reference) colloid (5 nm ND suspension with a negative zeta potential, 1 wt. %, Adámas Nano) was used as a DND reference in size distribution and spectroscopic characterizations.

Particle size distribution (PSD) characterization

Dynamic light scattering (DLS) was measured by a Zetasizer Nano (Malvern Panalytical) equipped with a helium-neon laser (633 nm); the scattering angle was 173°. The refractive index of bulk diamond (2.4), the viscosity of pure water (0.89004 mPa.s at 25 °C) was used to convert the measured intensity/size distributions to volume/size distributions. The concentration of ND was kept in 0.5-1.0 mg/mL range. To partially overcome inherently low resolution of DLS, every sample was analyzed by 50 measurements, each consisting of 10 runs of 10 s duration. Those 50 measurements were summed to provide a single PSD curve. Note that only SD-DND ref. and c1 fractions of HPHT O-NDs and SR O-DNDs could be reliably measured by DLS.

PSD of all the samples and fractions was further explored by *analytical ultracentrifugation* (AUC) measured by ProteomeLab XL-I equipped with the An-50 Ti rotor

(Beckman Coulter) using a sedimentation velocity experiment[25]. ND colloids in DI water were spun at 10000 – 30000 rpm at 20 °C and 100 – 200 scans with 0.003 cm spatial resolution were recorded in 2 – 6 min steps using absorbance and interference optics. Solvent density and viscosity values for water at 20 °C (ρ 0.99823 g/mL; η 1.002 mPa.s) were used, whereas NDs partial specific volume was estimated as inverse of diamond density with 0.2841 mL/g. The data were analyzed with Sedfit software using a c(s) continuous size distribution model [26] and recalculated to Stokes hydrodynamic radii and then to hydrodynamic diameter.

Small Angle X-ray Scattering (SAXS) was measured at the Fraunhofer Development Center X-ray Technology in Würzburg with an in-house build system. The c1, uc2 and uc3 fractions of both HPHT O-NDs, SR O-DNDs as well as the SD-DND reference were measured in vacuum using a custom build sample cell with a quartz capillary having 10 µm thin walls. Here, a combination of a high-power rotating Cu anode (λ=1.54 Å), a multilayer optics for monochromization, a collimation system with scatter less slits and a single-photon counting detector was used. To measure in a sufficient large Q-scale for the size distribution analysis, 3 different sample detector distances (SDD); 50, 600 and 1600 mm; were chosen and the integration time was 1h for each distance and for the background and calibration measurements. The SDD was calibrated using silver behenate (CAS: 2489-05-6, Alfa Aesar). Data treatment and analysis were performed with Nika [27] and Irena [28], which are freeware macros in Igor PRO. The 2D intensity data was reduced using water in the capillary as background, the transmittance of the sample and a glassy carbon standard from APS for absolute intensity calibration[29] was measured with the SAXS system. After the reduction, the 1D data of the different SDDs was stitched together, to receive a sufficient Q-scale. The size distributions were obtained using the fit routine 'Size Distribution' in Irena. The details of the SAXS data modelling are provided in

the Supplementary information. Compared to other procedures, which are used to obtain size distributions from SAXS experiments (e.g. indirect Fourier transformation[30] or unified Guinier-Porod models[31,32]), this method directly models the size distribution and thus allows a direct comparison of all samples as well as comparison with other PSD methods used.

The particle size and shape were analyzed by a *transmission electron microscope (TEM)* FEI Tecnai G2 20 with a LaB6 cathode at acceleration voltage 200 kV. The TEM is equipped with a CCD camera Olympus Veleta. Samples were prepared by immersion of a carbon coated copper grid in ND colloid.

Samples for *X-ray powder diffraction* were prepared by repeated dropcasting of ND colloids on a surface of a Si zero background sample holder (ZBH) to finally form a thin layer. All the as prepared samples on ZBH were then placed into the sample holders for XRPD analysis. Diffraction patterns were collected with the PANalytical X´Pert PRO diffractometer equipped with a conventional X-ray tube (Cu K_α radiation, 40 kV, 30 mA) and a linear position sensitive detector PIXcel with an anti-scatter shield. A programmable divergence slit set to a fixed value of 1 deg., Soller slit of 0.04 rad and mask of 15 mm were used in the primary beam. A programmable anti-scatter slit set to a fixed value of 1 deg., Soller slit of 0.04 rad and Ni beta-filter were used in the diffracted beam. Data were collected in the range of 35° - 55° 2theta with the step of 0.0131° and 5000 s/step producing a scan in about 10 hours. Such a long scanning time was necessary to get a desired signal to noise ratio that permitted to perform the line profile analysis. Qualitative analysis was performed with the HighScorePlus software package (Malvern PANalytical, The Netherlands, version 4.9.0) together with the PDF-4+ database. The line profile analysis was performed using routines implemented in the HighScorePlus software [33]. The 111 diffraction lines of diamond were fitted using the pseudo Voigt profile function with

split width and shape. No background subtraction was performed during the fitting procedure. Contrary, the background was determined in the range of 40° to 48° 2theta. The calculated values of integral breadths of 111 lines (B_{obs}) were then corrected for the instrumental broadening (B_{std}). The net values of integral breadths (B_{struct}) and the positions of diffraction lines were then entered into the Scherrer formula to get the appropriate crystallite size in the [1,1,1] direction. K (crystal shape factor) corresponding to cubic shape of particles (K = 1) as well as spherical shape of particles (K = 1.07) was used. The correction for instrumental broadening was performed with the NIST SRM660a standard (LaB_6) that was analysed with the same geometry and the B_{std} values were determined by the same procedure as for ND samples.

Spectroscopic characterizations

For *Fourier transform infrared* (FTIR) analysis, ND colloids were drop casted on a gold substrate and the water was evaporated by 20 min annealing in air at 200 °C. FTIR spectra were measured by SAGA (Specular Apertured Grazing Angle) technique (with 80° angle of incident light) using a N_2-purged Nicolet iS50 spectrometer equipped with a KBr beam splitter and an MCT-HighD detector cooled by liquid nitrogen. The optical absorbance was calculated in standard absorbance units as $A = -\log(R/R_0)$, where R is the spectrum of the analyzed material and R_0 is the reference (background) spectrum of gold substrate. In all cases, the spectra represent an average of 128 scans recorded with a resolution of 4 cm^{-1}. All the spectra were baseline-corrected.

Samples for *X-ray photoelectron spectroscopy* (XPS) analysis were prepared by dropcasting of ND colloids on sputtered Au substrates and after evaporation of the water

introduced into the AXIS-Supra photoelectron spectrometer (Kratos Analytical Ltd., UK) chamber. Survey and high-resolution core level spectra were measured using monochromatized Al Kα radiation (incidence photon energy was 1486.6 eV, exposed X-ray spot size was 0.7 × 0.3 mm^2). Photoelectrons were collected in a constant analyzer energy mode with a pass energy of 10 eV resulting in the overall energy resolution of 0.45 eV (measured on the Ag 3d5/2 line width). The X-ray incidence angle was 54.4^o, and the photoelectron emission angle was 0^o with respect to the surface normal. Samples were not sufficiently conductive, hence charge compensation was used during XPS measurements. All spectra were additionally calibrated to the binding energy of sp^3 phase in C 1s peak at 285 eV. Atomic concentrations were determined from the corresponding photoelectron peak areas after standard Shirley inelastic background subtraction and taking into account the relative sensitivity factors of elements. High-resolution spectra were fitted by KolXPD program using Gaussian functions.

Samples for *Raman spectroscopy* measurements were prepared by repeated dropcasting and drying of ND colloids on Au-coated silicon substrates. By this approach, solid ND deposits were formed and then analyzed. A Ib diamond single crystal (Sumitomo Electric) was used for calibration. Micro-Raman measurements were performed using three different instruments, that were partially described in detail elsewhere [15,34]. Whenever possible, various excitation wavelengths were used.

The first instrument was a Renishaw InVia spectrometer that allowed measurements in the visible (532 nm), near-UV (325 nm), and near-IR (785 nm) spectral ranges. It was equipped with an air-cooled CCD detector, different specific gratings (1200 and 2400 grooves/mm), and dielectric rejection filters. Using the 325 nm excitation, the low frequency cut-off was at about 250 cm^{-1}, and the full width at half maximum of the reference diamond single crystal was close

to 9 cm^{-1}. Thus, in the UV range, this spectrometer was at first used for a fast wide range overview of the samples. For this particular wavelength, the spectral resolution was too low to enable a detailed analysis of the Raman diamond line profile. On the other hand, as we will see in the following, this spectrometer enabled acquisition of the spectra even under very low irradiance.

The second instrument was a Jobin-Yvon T64000 triple monochromator spectrometer that allowed measurements in both the visible and UV spectral ranges. For that purpose, it was equipped with a UV-enhanced liquid-nitrogen-cooled CCD detector, two different confocal optics, and interchangeable gratings (2400, 1800, 1200 and 600 grooves/mm). This spectrometer was mainly used with the 514 and 325 nm excitations, in both its subtractive and additive modes. The additive (subtractive) mode allowed to study the diamond line profile in significant detail: whatever the excitation wavelength, the measured FWHM of the Ib reference diamond crystal was close to 1.9 cm^{-1}.

The third instrument was a Renishaw InVia spectrometer, equipped with Bragg rejection filters. The use of this type of filter allowed the acquisition of very low frequencies, down to about 15 cm^{-1}. Measurements were performed at 514 nm.

For all instruments, 50× objective (numerical aperture or NA = 0.75) and a UV-dedicated 40× objective (NA = 0.5) were used to focus the laser at the sample surface and collect the scattered light. A special care was taken to prevent unwanted temperature effect that may induce phonon peak downshifts, or even sample modification upon illumination. When working on nanoparticles sample heating is a well-known issue, that strongly depends on the optical properties of the particles, thus on the excitation wavelength.

For most of the samples examined here, overheating was clearly evidenced from a downshift and broadening of the diamond Raman first-order mode. To estimate sample temperature, we employed already published empirical relation for bulk diamond: $\Delta\omega = -1.075 \times 10^{-5}T^2 - 0.0077T + 1334.5$ cm^{-1}, where $\Delta\omega$ is the change in Raman phonon frequency upon heating, and T is the temperature in Kelvin [35]. The first measurements immediately showed that temperatures as high as 400 °C may be easily reached while using rather moderate laser powers, as low as few mW/μm^2. In addition, they also showed that laser-induced heating strongly depends on different parameters, such as the thickness of the deposit, or on the conditioning of the sample. Thus, for each excitation wavelength the incident laser power was accordingly minimized below 500 μW/μm^2 while finding a compromise between acquisition time and signal to noise ratio at the same time. Furthermore, the InVia instrument was modified to allow a line scan excitation on the sample. The line excitation instead of point excitation drastically reduced the irradiance of the sample while keeping rather high signal to noise ratio. Using such focusing conditions, it was possible to use power densities as low as 5 μW/μm^2 and reasonable acquisition time, between 60 s and 2400 s depending on the desired signal quality. Only these last conditions enabled reliable Raman analysis and discrimination of specific effects on some on the samples, DNDs in particular.

Using visible excitation wavelengths, Raman spectra of NDs were systematically superimposed on a strong photoluminescence (PL) background. The PL background has been roughly fitted by a polynomial function and then subtracted. However, it should be noted that this subtraction may be subjective. Moreover, in some cases, DNDs in particular, this PL background prevented the detection of orders-of-magnitude weaker Raman signals. Only the use

of 325 nm excitation, far from the maximum of the broad PL bands, enabled to record Raman spectra with a rather flat background for all the samples examined in this work.

Results

Particle size distributions

For any size-dependent characterization, accuracy of the PSD data is highly important, even more when the expected particle size is on the scale of few nanometers. Our results suggest that a single technique is often incapable to provide accurate and complete PSD data due to specific limitations of particular technique. We show here that a combination of several techniques (working on different principles) can provide a more comprehensive view and overall more accurate PSD. At the same time, suitable experimental conditions and limitations of particular technique are revealed.

Figure 1 shows PSD of the studied samples obtained by DLS (black), AUC (red), SAXS (blue, dashed blue) and average crystallite sizes obtained by XRD (green, orange). These techniques directly provided mass/volume-weighted PSD data (AUC, SAXS, XRD) or the data were recalculated to the mass/volume-weighted data (DLS). For DLS and AUC the obtained particle size formally corresponds to a particle hydrodynamic diameter, i.e. neat particle diameter plus twice a hydration shell thickness. The AUC data were obtained from sedimentation velocity that reflects size dependence of sedimentation rate, i.e. the bigger/heavier particles sediment faster than smaller/lighter particles. Briefly, the optical detector monitors temporal evolution of the sedimentation boundary of the colloidal solution under the application of centrifugal field.

The data are then converted to a hydrodynamic Stokes´ size distribution using the Svedberg equation[36]. Although AUC has a reputation of high-resolution technique with sub-nm resolution, as demonstrated on Au nanoparticles [37], its combination with another technique, such as TEM, is recommended to correct often inaccurate absolute size values [36]. Compared to AUC, DLS is low-resolution, yet broadly used technique, measuring time-dependent fluctuations in the scattering light intensity to determine translational diffusion coefficient, and subsequently the hydrodynamic diameter. SAXS is a method that uses X-ray scattering at small angles due to difference in electron density between the investigated particles and the surrounding medium. As such, SAXS data can be used for calculation of the volume/mass-weighted PSD. SAXS is regularly used for determination of a mean DND size or PSD [32,38,39] as well as for studying of aggregation and aggregate structures in various environments from hydrocolloids[30,31] to DND-polymer composites[40]. XRD provides an average crystallite size, more exactly a coherence length, obtained from the Scherrer equation using, among others, the full width at half maximum (FWHM) of diamond <111> diffraction line and K-factors corresponding to cubic (green) and spherical (orange) particle shape. Apart from the decreasing crystallite size, additional broadening of the diffraction line can be caused also by structural defects, micro strains in particular. Thus, the XRD-derived size values may not reflect the true particle diameter, the more the particle structure deviates from a perfect crystal. Figure 1a shows a schematic visualization of particle size as detected by the various employed methods.

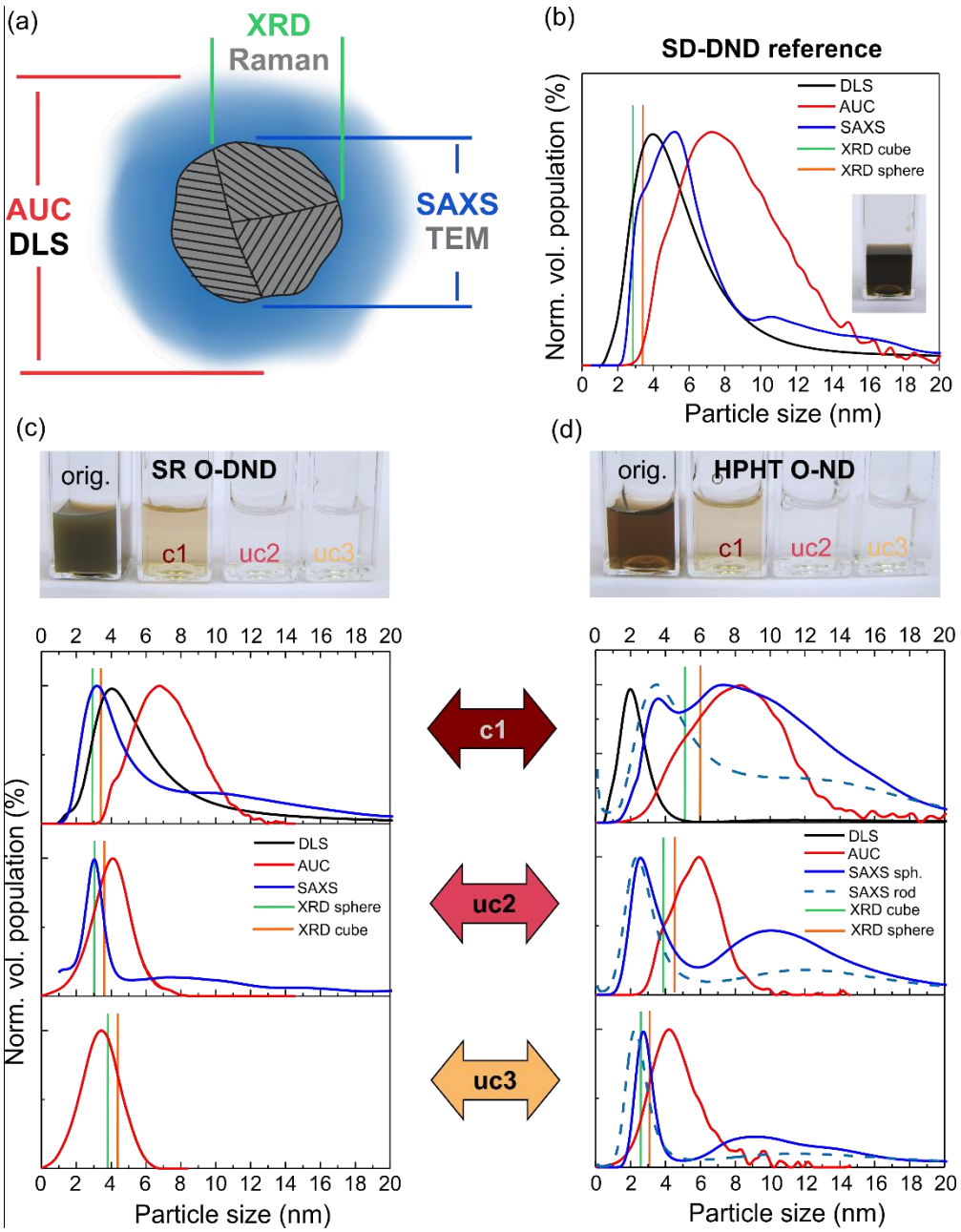

Figure 1. Schematic visualization of the size values as provided by DLS, AUC, SAXS, TEM, XRD and Raman (a). Volumetric size distributions of SD-DND reference (b), c1, uc2 and uc3 fractions of SR O-DNDs (c) and HPHT O-NDs (d) as measured by DLS (black), AUC (red), SAXS (blue for a sphere approximation, dashed light blue for a rod approximation) and XRD (green for a cube approximation, orange for a sphere approximation). Photographs show natural appearance of the original ND colloids and obtained fractions in glass cuvettes.

To better understand the contributions and limits of each PSD technique and relations between them we used a reference DND sample. This colloidal sample contains water-dispersed, well-deaggregated, conventional primary 3-6 nm DND particles which are characterized by a relatively narrow size distribution[1]. The sample is further denoted as the single-digit DND reference (SD-DND ref.).

Figure 1b shows volumetric PSD of the SD-DND ref. obtained by DLS, AUC, SAXS and XRD techniques as well as the brown-black appearance of the colloid in the inset image. All the employed techniques confirmed the single-digit character of the sample, which means that sub-10 nm individual DND particles represent a volumetrically dominant fraction. This is an important factor for further considerations. DLS mode size (i.e. the size with the highest occurrence, corresponding to the volumetric PSD peak value) of the SD-DND ref. sample is 4 nm (DLS hydrodynamic diameter) with a negligible occurrence of > 10 nm DND particles (or DND aggregates). The SAXS data show a minor population of approx. 3 nm DNDs a mode size of 5.2 nm, and a certain occurrence of > 10 nm DND particles and/or DND aggregates). The SAXS-derived mean size of the primary DND particles using our model agrees well with the sizes reported in previous SAXS studies[30,32,38,39]. It confirms the applicability of the used model. Overall, the SAXS and DLS data appear in a good agreement if we exclude the contribution of the hydration shell to the DLS data. In fact, such agreement indicates that the effect of hydration shell on DLS data is in our experiments negligible.

In contrast, the AUC data invoke a larger mode size of the reference SD-DND, peaking at 7.3 nm. Since the AUC was the only technique that was able to obtain PSD data of all fractions of the HPHT O-NDs and SR O-DNDs, it is important to understand the AUC data in relation to DLS and to SAXS.

We assume, that for quasi-spherical DND particles, the use of a sphere approximation is acceptable for all the three techniques. The presented results thus suggest that the hydrodynamic diameter obtained from DLS and AUC significantly differs. The DLS values seem not to be influenced significantly by the hydration layer and correspond more to the neat particle diameter (obtained independently e.g. by SAXS), an observation made also in some prior studies[7,41,42]. On the other hand, the AUC data seem to be more affected by the ND hydration shell or other effects. This may be caused by only microscopic-scale Brownian motion in DLS compared to macroscopic-scale sedimentation where the presence of hydration shell makes the particle heavier and thus bigger for AUC. Indeed, systematic discrepancies between AUC and DLS have been reported[24,43]. In both reports the AUC provided 2.1-2.3 times larger sizes of individual well-fractioned DNDs in sub-10 nm range than DLS. This difference was attributed to a non-ideal sedimentation behavior and/or a presence of relatively thick hydration shell around the hydrophilic NDs[24]. The discrepancy was mitigated by using a correction factor of 0.4 to normalize the AUC data to PSD obtained independently from DLS and AFM. However, we found inappropriate to use this correction factor in the present study. It would shift the AUC mode size of the reference SD-DND sample to 2.9 nm, which is obviously a too small value and such correction probably cannot be applied generally on all the samples. As a more relevant correction of the AUC data we propose subtraction of a water hydration shell from the AUC hydrodynamic diameter values. The thickness of the hydration shell around colloidal DNDs has been estimated to be around 1 nm (ca. 3-4 monolayers of water)[44]. Then, subtracting 2 nm from the AUC data shifts the mode size to 5.3 nm which is already in good agreement with the SAXS value as well as with the manufacturer´s specifications. Note that application of the analogous

hydration shell subtraction on the DLS data is not realistic since it would lead to 2 nm mode size. That would be in contradiction to all other methods including SAXS and TEM analyses.

Application of Scherrer equation on the XRD data of the SD-DND ref. sample results in 2.9 nm, 3.5 nm for a cubic and spherical shape approximation, respectively. The XRD values are the smallest compared to other employed techniques but they have been quite commonly obtained for DNDs by this technique[39,45,46]. It is the first indication that the XRD values derived for DNDs may not reflect accurate particle diameter due to some additional diffraction line broadening, e.g. due to presence of structural defects within individual particles.

The above PSD analysis of the SD-DND ref. by multiple techniques provides a robust foundation for characterization of the fractionated SR O-DND and HPHT O-ND samples. The PSD of the c1, uc2 and uc3 fractions of the SR O-DND sample obtained by DLS, AUC, SAXS and XRD techniques is shown in the Figure 1c. There is a relatively good agreement in the DLS and the SAXS data of the SR O-DND c1 fraction, similarly to the SD-DND ref. The DLS mode size is just below 4 nm. The SAXS mode size is 3.2 nm. Both methods suggest only minor occurrence of larger particles (or aggregates) up to 20 nm. The AUC mode size of 6.7 nm is again noticeably higher than the DLS and SAXS values. XRD values are 2.9 nm and 3.4 nm for the cube and sphere approximation, respectively.

PSD data of the uc2 fraction involve only the SAXS, AUC and XRD. DLS measurement of the uc2 and uc3 fractions (also of the HPHT O-NDs) led to very scattered size distribution data due to already too small particle size (scattering intensity scales up with r^6) together with a too low concentration [43]. Although SAXS data of the uc2 fraction already exhibit a large error (see Figure S2, S3) and thus can be taken only as an estimation, they still suggest narrowing of

the size distribution accompanied by decrease of the mode down to ~3 nm. AUC data follows the same trend providing the mode size of 4.1 nm.

SAXS measurement of the SR O-DND uc3 fraction was already impossible due to very low signal-to-noise ratio possibly caused by too low concentration and/or pronounced aggregation of the ultra-small DNDs in which the individual particles cannot be distinguished by SAXS under static conditions[31]. The AUC data are further shifted to smaller values compared to the uc2 fraction, showing the mode size of 3.4 nm. Although any size-dependence of the hydration shell thickness down to ~ 1 nm ND size is at the moment unknown, we may tentatively assume the mode size of neat particles in the uc3 fraction to be around 2 nm since the particles still form a colloidal solution and a hydration shell is present. The XRD-derived values show no clear evolution with decreasing size from SD-DND ref. to the SR O-DND uc2 fraction. Indeed, the XRD-derived crystallite sizes are 2.9-3.0 nm (cube) or 3.1-3.6 nm (sphere) for all the three SR O-DND fractions. Diffraction <111> patterns of all the samples are shown in Figure S1. Unfortunately, the ND quantities available for XRD analysis were very low, and thus they permitted to analyze the <111> diffraction line only. It is, therefore, impossible to deconvolute size effects and strain effects from one line only due to the fact that the line broadening could be a sum of instrumental part, size effects and strain effects. However, we succeeded to analyze the initial DND powder that has been used for preparation of the SR O-DND samples by size reduction and fractionation by (ultra)centrifugation. Here, we were able to measure an X-ray diffraction pattern in the angular range up to 147 deg (2theta, Cu radiation). It permitted to build a Williamson-Hall plot. We estimated here that the average coherent length is around 2.6 ± 0.3 nm (for cube shape) and the strain contribution about -0.4 ± 0.3 %. The detected strain was of tensile nature. Still, the magnitude of the contribution of strain effects to line broadening is close

to limits of precision that could be achieved for such samples. Interestingly, the Scherrer formula and using <111> diffraction only resulted in 2.6 and 3.1 nm for cube and sphere shapes, which is again very close to the SR O-DND c1-uc3 values and confirms XRD size insensitivity to DNDs.

Finally, Figure 1d shows the PSDs of the c1, uc2 and uc3 fractions of the HPHT O-ND sample obtained by DLS, AUC and SAXS techniques as well as average crystallite coherent length provided by XRD. As well as SD-DND reference and SR O-DND c1 samples, we evidenced a noticeable inconsistency in DLS, SAXS and AUC data of the HPHT O-ND c1 fraction. The difference between the DLS and AUC data is the largest in this sample. While the DLS data indicate the mode size of 2 nm and a very narrow PSD with low contribution of > 5 nm particles, the AUC data show rather broad PSD with mode size of 8.3 nm and some occurrence of > 14 nm particles. Similarly to AUC, SAXS indicates rather broad, bimodal PSD with peaks around 3.6 nm and 7.2 nm spanning up to 20 nm for spherical approximation. Additionally, when a rod-shape approximation was used to fit the raw SAXS data of the HPHT O-NDs it suppressed the bimodal character of the PSD and yielded mode size of 3.5 nm. Use of the rod-shape approximation is discussed further below. In any case, the AUC and SAXS data indicate that the PSD of the HPHT O-ND c1 fraction is broader and the ND mode size is bigger compared to the SR O-DND c1 fraction.

The SAXS, AUC and XRD analyses of the HPHT O-ND uc2 and uc3 fractions clearly evidenced i) the elimination of the larger particle population and thus increasing volumetric contribution of the sub-5 nm particles (SAXS) and ii) the shifting and narrowing of the PSD data (SAXS and AUC). The mode size values of the lower-size SAXS peaks are 2.5 nm and 2.7 nm for the uc2 and uc3 fractions (spherical approximation), respectively. The AUC mode size values

are 5.9 nm and 4.2 nm for the uc2 and uc3 fractions, respectively. Again, the subtraction of 2 nm hydration shell brings the AUC values close to the SAXS values.

In contrast to the DND samples, the size decrease in the HPHT O-ND samples is well documented also by broadening of the <111> diffraction line going from c1 to uc3 fraction (see Figure S1). As result, the average crystallite size decreases from 5.1 nm (cube) or 6.0 nm (sphere) for c1 fraction to 3.9 nm (cube) or 4.6 nm (sphere) for uc2 fraction and 2.6 nm (cube) or 3.1 nm (sphere) for uc3 fraction. These values and trends are in good correlation with the AUC (after water shell subtraction) and SAXS results as well as TEM results.

The volumetric mode sizes obtained by DLS, AUC and SAXS and the XRD-derived sizes corresponding to an average crystallite size are summarized in Table 1 for all the investigated samples. In the case of SAXS, values for the sphere (all samples) and rod (HPHT O-NDs only) approximations are given. In the case of XRD, values for the cube and sphere approximation are reported.

Table 1. Summary of the volumetric modes (DLS, AUC, SAXS) and average crystallite size (XRD) of the SD-DND reference, SR O-DND and HPHT O-ND c1, uc2, uc3 fractions.

Sample	DLS (vol. mode); nm	AUC (vol. mode); nm	SAXS sph. (vol. mode); nm	SAXS rod (vol. mode); nm	XRD cube; nm	XRD sphere; nm
SD-DND ref.	4.0	7.3	5.2	-	2.9	3.5

SR O-DND; c1	4.0	6.7	3.2	-	2.9	3.4
SR O-DND; uc2	-	4.1	3.0	-	3.0	3.6
SR O-DND; uc3	-	3.4	-	-	2.9	3.1
HPHT O-ND; c1	2.0	8.3	7.2	3.5	5.1	6.0
HPHT O-ND; uc2	-	5.9	2.5	2.4	3.9	4.6
HPHT O-ND; uc3	-	4.2	2.7	2.2	2.6	3.1

Direct imaging of the investigated particles by TEM was used to provide further corroboration of the particle sizes, shape, and atomic structure. TEM is regularly used to obtain PSD data of nanoparticles but due to highly local nature of such analysis, certain care should be taken to generalize such results. Another serious obstacle to retrieve reliable PSD data is often inherent aggregation of the nanoparticles on the TEM grid. This seems to be a rule for NDs and so far we are aware of only two attempts to overcome this problem[11,12]. Yet, even in the aggregated state TEM is capable to provide at least particle size range[47] and an estimation of the most frequent size in the sample.

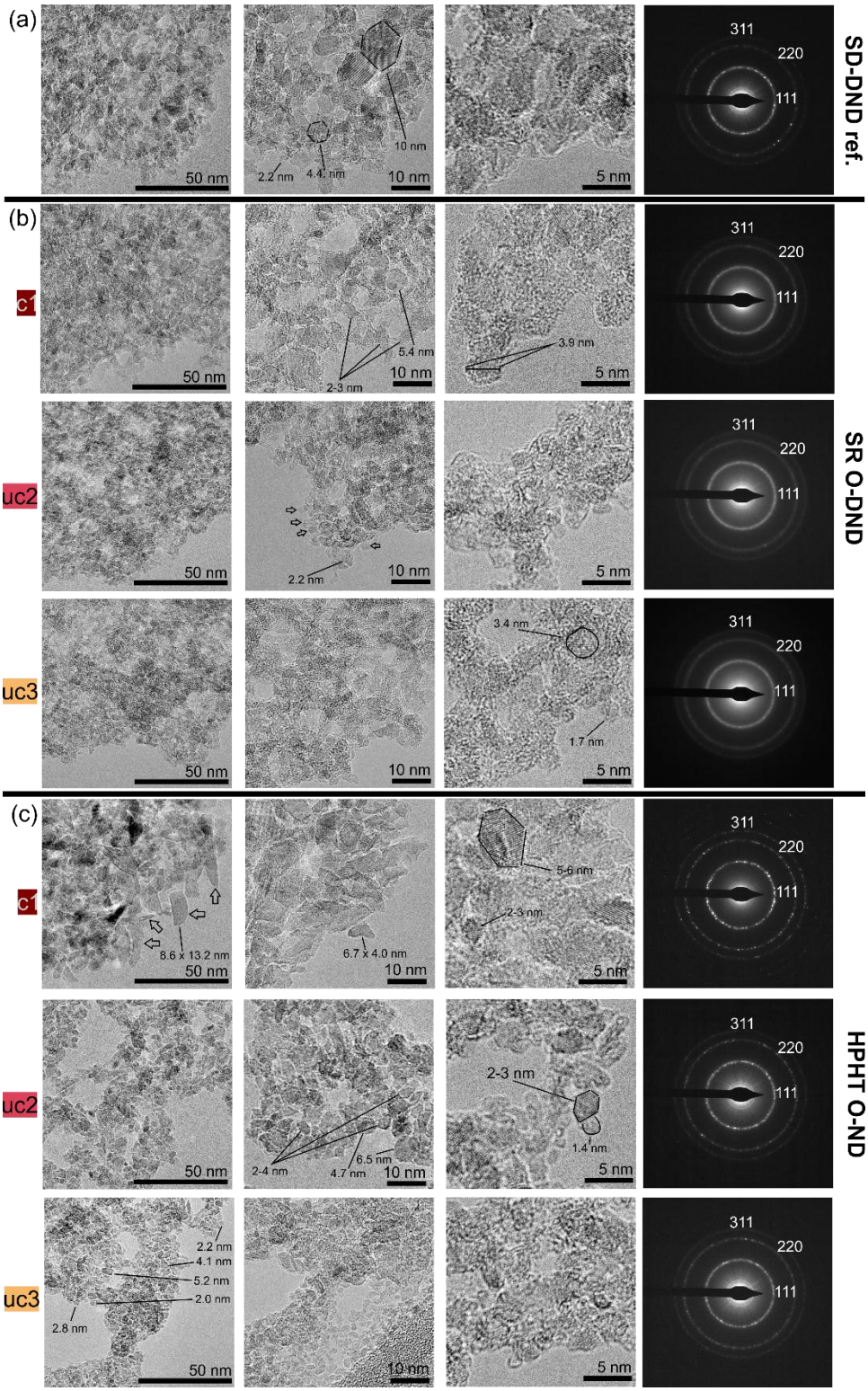

Figure 2. TEM image of the SD-DND ref. (a), SR O-DND c1, uc2, uc3 fractions (b), and HPHT O-ND c1, uc2, uc3 fractions (c).

Figure 2a shows TEM images of the SD-DND ref. sample. The TEM images confirms that the PSD is rather broad ranging from very small particles (1-3 nm) whose occurrence is relatively frequent up to rare ~ 10 nm primary DND particles. The most characteristic size seems to be in the range of 4-6 nm that agrees well with the PSD characterization above.

TEM images of the c1, uc2 and uc3 fractions of the SR O-DND sample are shown in Fig. 2b. In the c1 fraction all the particles seems to be below 10 nm, most of the particles are below 5 nm. Compared to the SD-DND ref. the particles are generally smaller which is in agreement with the previous report where a 2-3 nm thin layer was formed on Si using c1 fraction of hydrogenated SR DNDs[24]. It is, however, difficult to determine the size more accurately since the individual particles are hardly distinguishable. The TEM images of the uc2 and uc3 fractions of the SR O-DND sample indicate that the > 5 nm particles are completely suppressed and the most characteristic particle size is in the range of 1-4 nm. After drying out on the TEM grid, the particles in the uc2 and uc3 fractions often form chains that are composed of individual particles as the diamond lattice is clearly observable. Example of such chain is shown in the highest magnification (right column) in the uc2 fraction of the SR O-DND sample. In general, the TEM imaging showed that in all SR O-DND fractions the diamond crystal lattice is still present. This finding is confirmed also by the electron diffraction patterns that are shown in the right column in the Fig. 2. They all exhibit clear diffractions from <111>, <220>, and <311> planes.

TEM images of the c1, uc2 and uc3 fractions of the HPHT O-ND sample are shown in the Figure 2c. The TEM images reveal that apart from perhaps prevalent sub-10 nm particles, the c1 fraction of the HPHT O-ND sample contains also relatively large NDs up to 20 nm size. The particle shapes include rather frequent rod or splinter-like shapes with a high aspect ratio that largely deviates from the sphere approximation. Examples of such particles are noted by arrows

in the survey TEM image (left column) of the c1 fraction. Higher magnification reveals presence of smaller faceted particles with dimensions in the range of 4-7 nm as well as very small 2-3 nm particles. TEM images of the uc2 fractions of the HPHT O-NDs evidences the effect of ultracentrifugation: most of the particles are below 5 nm and particles > 5 nm are greatly suppressed. Further size reduction is achieved in the uc3 fraction where the characteristic size seems to be in the 2-4 nm range. It is best visible from the particle monolayer area denoted by the lines. Also, in the HPHT O-ND sample the highest magnification images (right column) as well as diffraction patterns clearly show the diamond structure of the particles down to 1-2 nm.

The PSD data (Figure 1) and the TEM analysis (Figure 2) of the SD-DND reference as well as of the SR O-DND fractions show mostly clear PSD trends and correlations between the employed techniques. In contrast, understanding the PSD data of the HPHT O-NDs is less straightforward. In the case of the c1 fraction, the most striking is the observed discrepancy of the DLS and other PSD data. Performance of DLS might be limited for polydisperse samples, very small particles (≤ 2 nm), or particles with irregular shapes. The detailed PSD characterization by AUC and SAXS as well as TEM imaging reveals that all these three issues occur in the HPHT O-ND c1 fraction. Therefore, the DLS results, suggesting nearly sole presence of sub-5 nm NDs, are highly misleading and obviously not valid.

After the reduction, all the SAXS data were at first analyzed with the total non-negative least square method using a sphere as the particle shape (blue curves in the Figure 1). The SD-DNDs and SR-O DND fractions can indeed be well approximated by a spherical shape, which is also confirmed by their TEM analysis. This results in good accuracy of the PSD data obtained by SAXS. In contrast, the HPHT O-NDs SAXS PSD data show an unexpected bimodal distribution when fitted by a spherical shape. TEM analysis (Fig. 2c) clearly showed that HPHT O-NDs often

have a high aspect ratio shapes. Thus, using the spherical shape, the first peak of the fits may in fact represent the diameter of the NDs and the second peak the length of the NDs. Critically, the lower size peak (high-q scattering) might also originate either from a ND surface texture[38] or the ND facets. It has been shown that implementation of the sp^2-C texture roughness to the SAXS data modelling of DNDs led to shift of the DND mean size from 4 nm to 6 nm[38]. In the present study, a significant contribution of the surface texture was not assumed due to following reasons: its contribution should be more or less constant throughout the HPHT O-NDs fractions. Yet, the size decreases from ~3.5 nm for c1 to ~2.5 nm for uc2 which, in accordance with other techniques (AUC, XRD and TEM), corresponds rather to dimensional decrease and it thus assigned to the whole ND particle. Moreover, TEM images (Figure 2) suggest rather smooth surface of the HPHT O-NDs as well as DNDs without frequent occurrence of shell-like features or protrusions. Finally, in the high-q region ($q > 0.3$) the intensity errors and the small intensity difference between the background and the scattered photons of the small NDs between 0.1 and 0.2 $\frac{1}{\text{Å}}$ don't allow us to do any statements about any surface roughness. SAXS data, SAXS data with subtracted background, and the fits using spherical shape are provided in the Supplementary information (Figure S2, S3).

Additionally, the HPHT O-NDs SAXS data were fitted using a rod shape (light-blue dashed curve in Fig. 1b). The length was specified to 110 Å for all fits, which is not far from maximum of the second peak in the spherical size distribution fit. Comparing the two fits, it is obvious that the second peak decreases significantly for the rod approximation. The second peak does not disappear completely because the length of the rod like particles is fixed in the fit but it has some distribution in reality. Overall, the rod shape approximation leads to suppression of the unusual bimodal PSD obtained by a spherical approximation as well as to a minor shift of the

mode sizes to smaller sizes. Since the HPHT O-ND particle shapes are indeed quite diverse, the two applied approximations (spheres and rods) may be considered as two "exemplary cases" in our attempts to obtain accurate SAXS PSD. Still the model fits the experimental data very well as shown in the Supplementary information. Similarly, application of the sphere and cube approximation to the XRD data provided some range of the average crystallite sizes that should correspond to average particle sizes for monocrystalline HPHT O-NDs. For the following spectroscopic characterization, it is important to conclude here that the ultracentrifugation enabled us to isolate the sub-5 nm ND with average particles in the range of 2-3 nm for the uc3 fraction of both detonation and HPHT NDs.

This agrees well with the already published results employing ultracentrifugation as the method for DND fractioning where a special attention was paid to obtain primary DND particles. For example, it has been shown that ultracentrifugation of a DND colloid with DND of standard size (2-6 nm) at 215,000 × g for 3 hours resulted in very diluted colloid containing very low population of approx. 2 nm DNDs [48]. Schmidlin et. al [49] reported mainly individual DND particles with a diameter between 2 and 4 nm observed by AFM after 30 min ultracentrifugation at 350,000 × g. Usoltseva et al. [50] reported mean size of 3.5 nm after ultracentrifugation at approx. 200,000 × g for one hour. From the published data it can be assumed that ultracentrifugation at 200,000-300,000 × g applied from tens of minutes to hours, i.e. similar to our conditions, is capable to isolate the smallest sub-4 nm DNDs fraction present in the colloids in spite of no pre-centrifugation step. To our knowledge, there is no such report for HPHT O-NDs fractionation. Yet, due to the similar surface chemistry and colloidal properties after the oxidation by annealing in air [12], similar PSD can be expected after such ultracentrifugation. Our results confirm this hypothesis.

Recently, spontaneous formation of DND particles aggregates in colloids was shown and studied by cryo-TEM and SAXS experiments[30,31]. Although we cannot exclude such aggregation in our samples (which indeed sometime occurs, see the SAXS data), we suggest that these aggregates consist of only weakly bound particles and can be broken by a force e.g. by centrifugation or sonication. There is quite obvious support for this assertion. First, the volumetric mode size decrease of all the investigated samples is here well-documented independently by SAXS, TEM, XRD and AUC. This indicates disruption of the aggregates during centrifugation and proves that the (ultra)centrifugation can still be used to fractionate the HPHT O-NDs as well as SR O-DNDs down to few nm. Second, there are also numerous reports showing individual DND particle deposition on a substrate after simple dropcasting[49] or ultrasonic bath-assisted seeding [24,41,42,51] which confirms that individual NDs can exist in the colloidal solution and/or the weakly bound aggregates can indeed be broken up by an external force.

Chemical composition and bonding configuration analysis by XPS

When the PSD were reliably characterized, chemical composition and bonding configuration of the DND and HPHT size fractions were analyzed by XPS. Table 2 shows atomic concentrations of O, N and C in the ND samples depending on ND origin, surface chemistry and (ultra)centrifugation treatment, i.e. size. In both HPHT O-NDs and SR O-DNDs samples the concentration of oxygen varies between 11 at.% – 16 at.%. Relatively high oxygen content results from oxidation during the air annealing treatment and it increases with decreasing particle size due to increase of surface-to-volume ratio, i.e. most of the oxygen comes from

oxygen-rich surface chemical groups. This assertion is reflected also by O/C ratio. Some of the oxygen might come also from surface-adsorbed water.

Nitrogen is present in the SR O-DND samples as a relic of detonation synthesis of N-rich energetic compound such as TNT. Noticeably, we did not identify any clear trend in nitrogen concentration with decreasing DND size or surface treatment: concentration of N remained similar for all SR DND samples. Therefore, nitrogen is homogeneously embedded in a whole volume of SR DND samples. In contrast to SR O-DND samples, the nitrogen content in HPHT O-NDs was close to the background intensity.

Au substrate photoelectron intensities were present in the spectra measured on the HPHT O-NDs uc2 and uc3 samples. Thickness of these sample was smaller than the thickness of SR O-DND samples and therefore emission of Au substrate was resolved. A thickness of HPHT O-NDs films was decreased with NDs particle size (Au concentration has increased). The measurement on such thin films (including substrate contributions) was necessary since we were not able to compensate the surface charge on thicker HPHT O-NDs uc2 and uc3 films.

Table 2. Chemical composition as measured by XPS

Sample	Atomic Concentration (±0.5 at.%)				Ratio
	O	N	Au	C	O/C
HPHT O-NDs_c1	11.6	0.1	-	88.3	0.13

HPHT O-NDs _uc2	16.1	-	1.8	82.1	0.20
HPHT O-NDs _uc3	15.5	-	4.1	80.4	0.19

SR O-DND_c1	11.6	2.4	-	86.0	0.14
SR O-DND_uc2	16.0	2.8	-	81.2	0.20
SR O-DND_uc3	17.6	2.3	-	80.1	0.22

Figure 3 shows deconvoluted C 1s, O 1s and N 1s spectra of HPHT O-NDs and SR O-DNDs samples. The C 1s spectrum of HPHT O-NDs c1 consists of sp^3 hybridized C (diamond phase), sp^2 hybridized C (non-diamond carbon), and C bonded to oxygen atoms (C-O, C=O). Line shape of the HPHT O-NDs c1 spectrum is similar to oxidized nanocrystalline diamond samples[52]. In spectra of HPHT O-NDs uc2 and uc3 a new component C_{int} appears at lower binding energies at 283 eV. Such low binding energies could be related to carbides. However, no other element that could form carbide was detected in the samples. Instead we found, that position of the C_{int} component did not depend on charge compensation parameters similar to Au core level positions (i.e. it is electrically conductive) whereas overlayer C 1s components were shifted with different electron beam voltage. In addition, area of C_{int} component and Au concentration in Tab. 2 were increased with ND size decrease (Au concentration was 1.8 at% for uc2 and 4.1 at% for uc3; C_{int} concentration was 5.3% for uc2 and 13.4% for uc3, see Tab. 1 and Tab .2). Therefore, there is a

clear correlation between C_{int} component area and Au concentration. We can thus relate the C_{int} component to carbon at Au interface.

The C 1s spectra of SR O-DND sample in Figure 3 b) are significantly broader than HPHT O-NDs ones and contain sp^3, sp^2, C-O, C=O as well as an additional component C-N/C_{def} between 285.8 eV – 286.0 eV. This component has been already described and identified as contribution from a defective, C_{def}, carbon sp^3 phase and/or C-N bonds [53]. Since atomic concentration of N is only approx. 2 at.% in DND samples the C-N bonds alone cannot be responsible for the relatively large area of this component in the C 1s peak. It is thus reasonable to expect that this component involves two contributions from both defective carbon and C-N bonds. We are aware of the fact that introduction of this component might seem redundant. But without this approach we were not able to obtain reasonable fits and correlation to oxygen atomic concentration obtained from the survey spectra.

The different C 1s spectra also highlights structural differences between the HPHT and detonation NDs in terms of elemental purity (nitrogen) and/or crystallinity as suggested by the XRD data and shown in detail by Raman spectroscopy further below. The C 1s spectra of SR O-DND fractions are quite similar without any pronounced evolution with decreasing size, which again correlates with XRD and Raman analysis. Small differences in intensities were evaluated and included in Tab. 3. The sp^2/sp^3 bond ratio slightly increases from c1 to uc3 fraction. Still, a major fraction of the SR O-DND and HPHT O-NDs samples down to uc3 fraction remains in the diamond (sp^3) phase.

The O 1s deconvolution of the HPHT O-ND samples revealed dominant contribution of C-O bonds with binding energy of 532 eV and minor contribution of C=O and C-OH/H_2O

components. In the case of the SR O-DND samples, the C-O bonds are still dominant, but the C=O component increases with decreasing size of the DNDs. Note that the C=O components can overlap with N-C=O bond components, but we were not able to resolve it. C=O component increase with centrifugation time is not due to nitrogen bond increase (N concentration remained similar for all SR O-DND samples).

Deconvolution of the N 1s peak of the SR O-DND sample revealed presence of two bonding states of DND-incorporated nitrogen. In the literature, the N 1s component at 399 eV was assigned to substitutional nitrogen in carbon sp^3 or sp^3/sp^2 configuration [39,54] or to nitrogen atoms incorporated in a graphite edge structure [55] (N_1 component). The higher binding energy component (402.5 eV) was assigned to nitrogen in graphite edges, in this case nitrogen that is connected to three neighboring carbon atoms at the edge [55] (N_2 component). According to Hellgren et al. [56] the 402.5 eV component corresponds to quaternary N substituted in a graphitic environment. Here, we revealed that nitrogen concentration is preserved independently on sp^2/sp^3 ratio variation or NDs size variation. Therefore, constant nitrogen concentration indicates homogeneous incorporation of N into NDs particles during detonation production process.

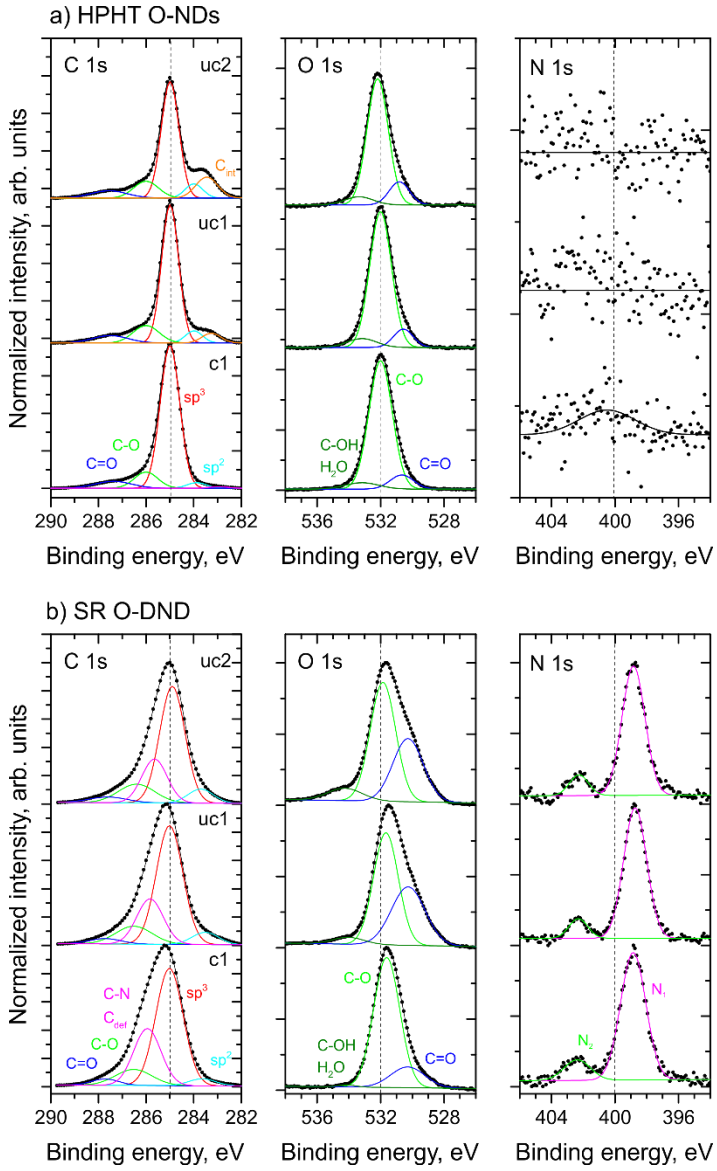

Figure 3. Dependence of C 1s, O 1s and N 1s core level spectra of HPHT O-NDs (a), SR O-DNDs (b) samples on size/centrifugation parameters. Experimental data and fits are marked by symbols and lines, correspondingly. Different components are colorized and explained by the text.

Table 3. Relative bond concentrations obtained from C 1s component areas.

	Concentration, rel.% (±1.5 rel.%)					Ratio
Sample	sp^2	sp^3	C_{int}	C-O	C=O	sp^2/sp^3
HPHT O-ND c1	3.0	78.3	0.8	10.7	7.2	0.04
HPHT O-ND uc2	6.0	68.0	5.3	13.1	7.6	0.09
HPHT O-ND uc3	7.3	59.5	13.4	12.1	7.7	0.12

	sp^2	sp^3	C-N/C_{def}	C-O	C=O	sp^2/sp^3
SR O-DND c1	3.4	56.1	27.3	10.2	3.0	0.06
SR O-DND uc2	5.9	57.3	21.9	11.9	3.0	0.10
SR O-DND uc3	6.7	55.6	20.9	12.8	4.0	0.12

XPS is the only method used in this work that can retrieve semi-quantitative bond concentrations. Relative concentrations of carbon bonds were derived from the C 1s component peak areas (Tab. 3). The sp^2/sp^3 bond ratio increases with decreasing particle size for all samples. In other words, smaller particles involve more non-diamond carbon phase and less diamond phase. Nevertheless, even in uc3 fractions of both SR DND and HPHT O-ND samples a major phase is still diamond phase and the sp^3 C concentration is rather similar for all uc3 ND samples.

The relative concentration of oxygen bonds (C-O and C=O) correlates with oxygen atomic concentrations. The C-O and C=O bond concentrations increase from c1 to uc3 fraction. It is due to particle size decrease that correlates with atomic concentrations (C 1s, O 1s core level areas). Relative concentrations of C_{def}/C-N bonds in SR O-DND samples (between 20% - 30% of C 1s area) are quite high and, as mentioned above, cannot by related to C-N bond only (N concentration is 2-3 at.% only). Therefore, the major contributions probably come from a defective sp^3-C or sp^3-sp^2 mixed phase, characteristic for DNDs.

Infrared spectroscopy

Because of its high sensitivity to various surface functional groups[57], FTIR spectroscopy has been used to complement the characterization of surface chemistry and its possible size-dependence on both HPHT O-NDs and SR O-DNDs. On the other hand, this method is known to be rather insensitive to sp^2 C=C bonds. All size fractions of HPHT O-NDs (Figure 4a) and SR O-DND (Figure 4b) showed absorption bands linked to the oxygen-containing surface groups as a result of the air annealing treatment[12]. A complete description of FTIR spectra, shown in Figure 4, is not yet completely clear. In particular, for defective or nitrogen-containing particles such as DNDs, the so-called "fingerprint" region of the spectra (900–1500 cm^{-1}) is often difficult to interpret because many of the expected contributions from the diamond core itself (defect-induced one-phonon diamond spectrum) and from the different O-related surface terminations are strongly overlapping. The high frequency part of the spectra typically brings clear information on the presence of surface C-H_x (~2800-3000 cm^{-1}) and -OH (~3000-3600 cm^{-1}) bonds. Unexpectedly, the C-H_x stretching features were identified in all the samples despite all

the NDs were oxidized by annealing in air well above the temperature of C-H_x bonds oxidation[10]. Moreover, their signal increases with the decreasing ND size from c1 to uc3 fraction. We attribute them to a hydrocarbon contamination since the same feature has been detected in the background spectrum of dropcasted water residual (not shown) and it is thus more pronounced in the much less concentrated uc2 and uc3 fractions. The presence of -OH bonds can be attributed to hydroxyl surface terminations and/or adsorbed water[58] with the corresponding bending mode often detected at about 1620 cm^{-1}, which is the case also here. The surface hydroxyls are not easily distinguished from those from adsorbed water molecules when measured at ambient conditions[58]. As the samples were dried for 20 min at 200°C prior the measurement the content of the adsorbed water had been significantly reduced. Still some of the detected –OH bonds may come from the surface-bound water[10,59]. Carbonyl C=O bonds are clearly identified from their stretching modes in the 1660-1800 cm^{-1} range. According to a position of the band, it is related to surface ketones, carboxylic acids, lactones or anhydrides[60]. Because the pH of the starting HPHT O-ND and SR O-DND 10 mg/ml colloids was acidic (pH ≈ 3.5) at least part of the C=O comes from the carboxylic acids or related groups that may hydrolyze in water such as lactones or anhydrides. The area below 1500 cm^{-1} is a combination of various stretching vibration of C–O and C–O–C groups, yet possibly overlapped with intrinsic absorption of diamond. Especially the maximum at ~1100 cm^{-1} is usually ascribed to ether groups [61] but appear also in Ib diamond [62]. Also, the diamond lattice vibration at ~1330 cm^{-1} corresponds to the first order Raman band (C-C vibrations of sp^3-hybridized carbon) and is typically inactive in IR. The appearance of the this band in the FTIR spectra can be explained by the disturbance of the diamond lattice zero dipole moment by more electron-negative nitrogen atoms impurities[63] which in case of regular DNDs typically reach 2 at.%. Due to only trace amount of nitrogen in the HPHT O-NDs the peak is not

identified in their FTIR spectra. Since the nitrogen is homogeneously distributed throughout the DNDs [39,64] this band can be considered as a signature of the diamond lattice presence. This band is easily resolved in the hydrogenated DND due to its smaller overlap with C-H_x bonds. In SR O-DNDs, this band can still be resolved as a shoulder and a peak in the SR O-DND c1 and uc2 fraction, respectively. In the spectrum of the uc3 fraction the peak is already barely noticeable due to increase of the surface-to-volume ratio and overlap with the surface chemical groups.

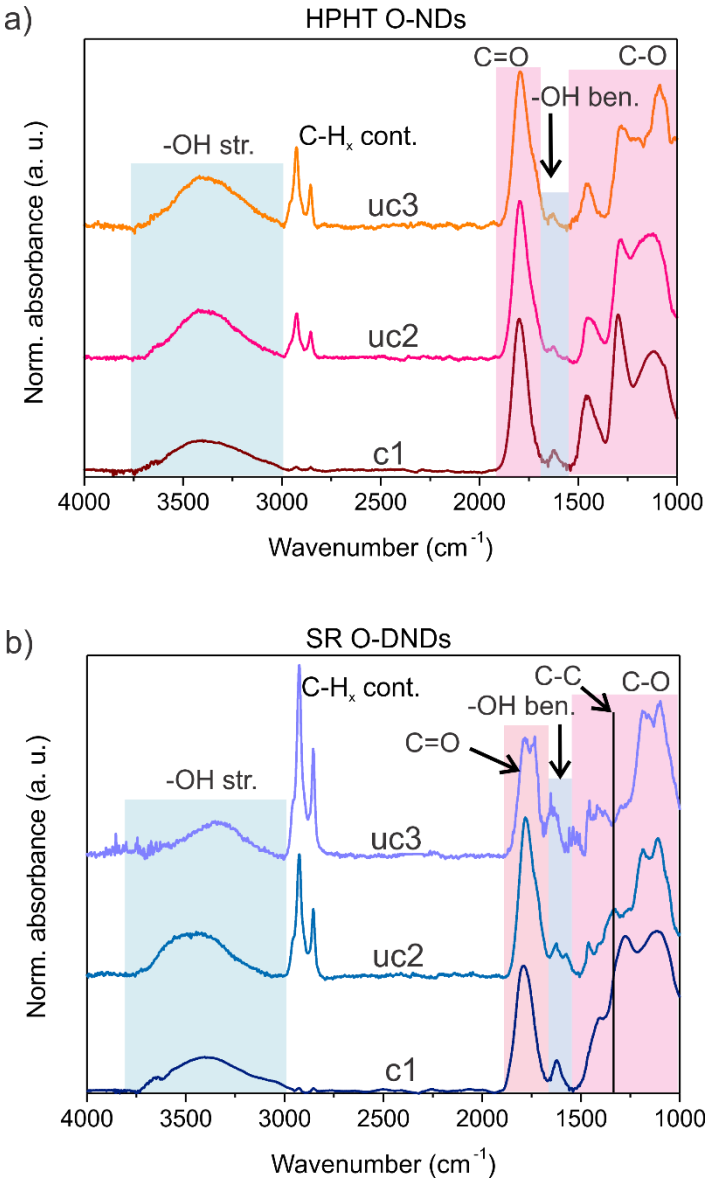

Figure 4. Size-dependent FTIR spectra of HPHT O-NDs (a) and SR O-DNDs (b).

The comparison of the FTIR spectra of c1 fractions of HPHT O-NDs and SR O-DNDs shows that the surface chemistry of these two ND kinds in this size range is relatively similar[12]. There are only small differences in the relative absorption of individual bands in the region 1500-1000 cm^{-1}, possibly caused by the higher intrinsic absorption of DNDs (e.g. the ~1330 cm^{-1}

band). With decreasing size, however, the FTIR spectra suggest some surface chemistry evolution in both ND kinds (HPHT O-NDs and SR O-DNDs). First, there is an apparent broadening of the C=O band with increasing contribution of a ~1740 cm^{-1} component from c1 to uc3 fraction in both HPHT O-NDs and SR O-DNDs. In the most extreme case (SR O-DND, uc3) the C=O related feature clearly splits in 1780 and 1740 cm^{-1} components. This may signalize appearance of anhydrides because these are characteristic by C=O band with two frequencies. Also rearrangement of the surface functional groups due to increase of the surface curvature with decreasing ND size may be assumed since the spectral position of the C=O band is sensitive to geometrical arrangement of the C=O containing moieties as well as degree of oxidation.

Second, in SR O-DND the –OH bending mode at ~ 1620 cm^{-1} in the c1 fraction also splits in two bands at ~1640 and ~1540 cm^{-1} in uc2 and uc3 fractions. This is not clearly observed in the HPHT O-NDs. A multicomponent –OH bending mode has been observed on hydrogenated DND[10,59,65] and assigned to on unusual hydration structure due to an electron accumulation at the hydrogenated DND−water interface[59]. Unexpected observation of this effect on ~ 3 nm or smaller oxidized DNDs may signalizes change in the electronic properties of the SR O-DNDs with decreasing size.

Finally, the absorption feature at 1280 cm^{-1} possibly coming from C-O stretching of carboxylic acids decreases its intensity from c1 to uc3 fraction in both HPHT O-NDs and SR O-DNDs. Such behavior may, in principle, results in a reduction of highly negative zeta potential of oxidized NDs which appears due to presence of carboxylic groups[7].

Thus, both HPHT O-NDs and SR O-DNDs seem to undergo a change in surface chemistry with reducing size. This assertion is supported by the fact that specific combinations of oxygen-

related groups are needed to fit on the nanodiamond surfaces as shown in several computational studies[66,67]

Size dependent Raman spectra of nanodiamonds

Successful isolation of sub-5 nm NDs of both DND and HPHT origin provides us a unique opportunity to elucidate some persisting issues, namely the effects of size, crystallinity (level of lattice and structural defects) and surface on the Raman spectra of NDs.

Figure 5 shows representative examples of Raman spectra of HPHT O-NDs (c1 fraction) and SD-DND reference sample obtained at 325 nm. Here, only the first-order frequency range is displayed, all the features observed in the 2000-4000 cm^{-1} range were of very weak intensity and did not bring any crucial information. These data were plotted as reduced Raman spectra in order to be compared to the calculated and measured diamond vibrational density of state (VDOS) [68]. Here, the reduced Raman spectrum $I_R(\omega)$ is given by:

$$I_R(\omega) = I(\omega)/(\frac{1 + n(\omega, T)}{\omega})$$

where ω is the Raman shift, $I(\omega)$ the measured intensity and $n(\omega,T) = (exp(h\omega/kT)-1)^{-1}$ the Bose-Einstein distribution function and T the temperature [69]. Such a correction removes thermal occupation effects from the measured Raman signal.

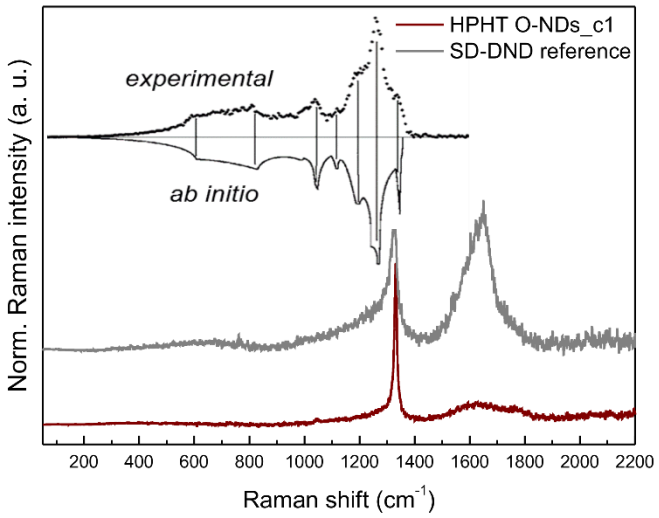

Figure 5. Reduced Raman spectra of the HPHT O-ND c1 and SD-DND reference obtained with 325 nm excitation. The inset shows the measured and calculated diamond vibrational density of state [68].

Although the Raman spectra of both types of NDs exhibit both "low" and "high" frequency features as already observed and discussed elsewhere [8,15–22,34] it is immediately apparent that both types of NDs provide significantly different Raman spectra. Information concerning the core of the nanoparticles may be found in the 0 and 1335 cm^{-1} range, i.e. below the cutoff frequency of the VDOS. In this frequency range, the first information is obviously given by the first-order diamond Raman line close to its expected position at about 1330 cm^{-1}. The diamond peak of the HPHT O-NDs c1 sample is significantly narrower and closer to the bulk diamond position than that of SD-DNDs ref. sample. Besides the diamond peak, broad low frequency features can also be observed in the 100–1300 cm^{-1} range. In particular, a shoulder is noticeable on the low frequency side of the diamond Raman line, peaking at about 1250 cm^{-1}, especially apparent for the SD-DND reference sample. Above the diamond cutoff frequency, a broad band rising between 1400 and 1800 cm^{-1} was observed for both types of NDs that give

some information on the non-diamond, sp^2-hybridized carbon. It might be composed of different, perhaps three, overlapping peaks at about 1580–1600, 1650 and 1750 cm^{-1}. Most often, this broad band is further denoted as "G" band [70,71] as this is for example the case for amorphous carbon layers. In the following, we will keep this notation, even though it may not perfectly reflect its complex character, and may not adequately describe the NDs surface chemistry. The two types of NDs greatly differ not only in the ratio of the diamond-to-G band intensity but also in the structure of this complex band.

We at first focused on the "G" line evolution with size reduction from c1 to uc3 fraction for both types of nanodiamonds.

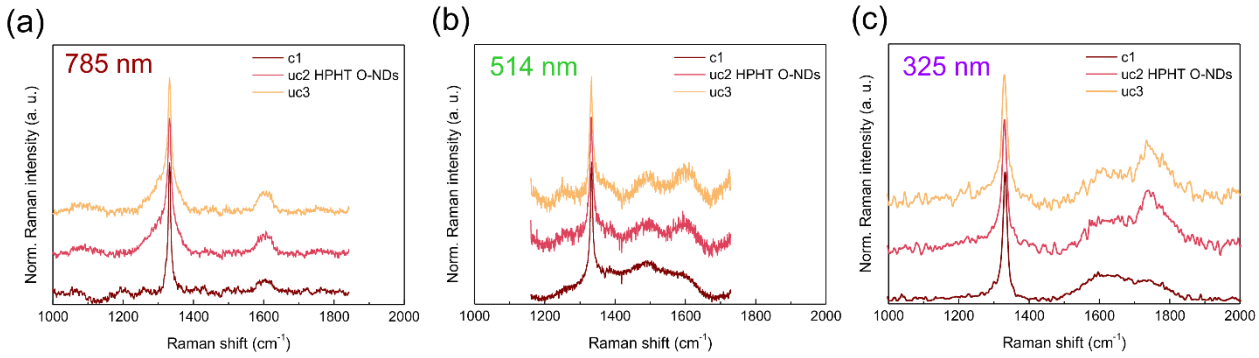

Figure 6. Multi-wavelength Raman spectra of the HPHT O-ND c1, uc2 and uc3 fractions obtained by 785 nm (a), 514 nm (b), and 325 nm (c) excitation.

The three HPHT O-NDs fractions were examined by 785 nm, 514 nm and 325 nm excitation wavelengths. The corresponding spectra are shown in Figure 6 after crude subtractions of the PL background and normalization to the diamond line intensities. The spectra are dominated by the first-order diamond Raman line, roughly peaking close to its expected position, at about 1330 cm^{-1}. The other spectral features clearly involve the so-called "G" and "D" bands, peaking at about 1350 and 1600 cm^{-1} for the 532 or 514 nm excitation. These features, and their frequency

evolution as a function of the excitation wavelength unambiguously identify defective or finite-size graphite[63], with dimensions in the nm range. Here, we emphasize that the disorder-induced "D" band is observed at about 1320 cm^{-1} at 785 nm, but must not be confused with the T_{2g} mode of the diamond.

As can be seen from the Figure 6, the graphite signature in HPHT O-NDs is only barely observable for all the fractions using different excitation wavelengths. This shows that the HPHT NDs can be prepared in a very pure state down to the size of several nanometers. For such low particle sizes (<20 nm in all cases), we do not expect large differences in probed volumes caused by the large difference in absorption coefficients of graphite and diamond: both graphite and diamond are therefore probed completely. In such a case, the graphite and diamond relative contents, characterized by the "G"/T_{2g} intensity ratio, may give an estimate of the relative concentration of the two phases. Using the commonly adopted factor of about 50 between the graphite and diamond scattering cross sections for excitations in the green spectral range, we conclude that the graphite content in all samples is rather low, a few % at most, and only minimally depends on the particle size distribution, see Fig. 6a and 6b, in which no strong intensity variations of the graphite G mode are observed . This content corresponds to values extracted from the XPS analysis. However, these analyses cannot identify whether the graphite is present in the form of isolated particles, as inclusions in the diamond lattice or as a defective shell surrounding the particles. Graphite most probably arises from the synthesis process itself, in the form of non-transformed, unreacted raw material. For comparison, see the data obtained for another HPHT ND batch prepared with identical conditions, and the corresponding discussion in Figure S5, supporting information (SI). Graphitic carbon is thus the main non-diamond carbon

impurity that can be present in the HPHT ND samples, even after extensive purification treatments by e.g. annealing in air [12].

Although the Raman spectra in Figure 6a-b shows that the HPHT O-NDs are almost graphite-free, a wide signal around 1600 cm^{-1} is observed when the analysis is carried out at 325 nm (Figure 6c). This signal cannot be attributed to the graphite contamination, since its accompanying "D" band is not observed around 1405 cm^{-1}. Moreover, even if the accuracy remains weak, line fitting procedures (not shown) strongly suggest that the mean line position is now peaking beyond ca, 1610 cm^{-1}. There are no clear trends in the intensity evolution with the reduction in average size. We can hypothesize that this signal tracks some specific sp^2 surface reconstruction, appearing possibly after a ND surface modification by the UV illumination.

Another spectral feature is systematically observed at about 1750 cm^{-1} while using an excitation at 325 nm. This component is the only clearly size-dependent feature in the HPHT O-NDs spectra with obvious increase with the decreasing particle size. This feature finds its counterpart in the FTIR spectra, and is assigned to carbonyl C=O groups [15,18]. Its evolution confirms the increase of the surface-to-volume ratio as the carbonyl groups are located at the surface of the NDs.

Finally, the spectra given in Figure 6b obtained by 514 nm excitation show various repeating maxima in the 1000 – 2000 cm^{-1} wavenumber range. They arise as interference-like pattern due to a response function of the Raman instruments. They are the more observable the weaker the Raman signal and the more intense the PL background are. This interference pattern stands out after subtraction of the PL background and, therefore, illustrates all the subjectivity of

such corrections. This may explain the variability observed for the three different samples, while the uncorrected spectra look similar. This effect must not be confused with real Raman signals [72].

In contrast to HPHT O-NDs, the multi-wavelength analysis of the SR O-DND samples was more difficult. In particular, when using 785 nm and 514 nm excitation wavelengths, it was impossible to discriminate with certainty the weak Raman signal from the huge PL background, increasing with the decreasing particle size. This is for example demonstrated in the Figure S6 where raw as well as baseline-subtracted spectra of the SR O-DND sample set are shown. Clearly, the Raman scattering signal decreases from c1 to uc3 fraction due to the increase of the surface (PL) to volume (Raman) ratio. The same was observed for HPHT O-NDs. This was not entirely the case for the ~5 nm SD-DND reference sample and partially for the c1 fraction. Still, in agreement with previous works [15,18,23], it was possible to obtain these spectra using the 325 nm excitation. These spectra are shown in Figure 7 after a baseline-correction and normalization to the diamond line intensities. The shape of all these spectra still perfectly corresponds to the one we know for conventional detonation NDs, see the grey reference spectrum in the Figure 7, and Refs [15,18].

Upon DND size reduction from SD-DND ref. to SR O-DND uc3, no clear evolution of the spectra could be evidenced, within the exception of a noticeable increase of the 1750 cm^{-1} component, already assigned to carbonyl surface moieties. As observed also for HPHT O-NDs, its intensity increases with decreasing particle size. On the other hand, the observed invariance of the "G" band shape on the size reduction suggests that this band has to be at least partly associated with bulk-like sp^2-C defects which have been indeed identified in the boundary regions located between discrete crystallites or crystalline domains within a DND particle[47]. For a more complete discussion of the origin of this signal, see[15], and references herein.

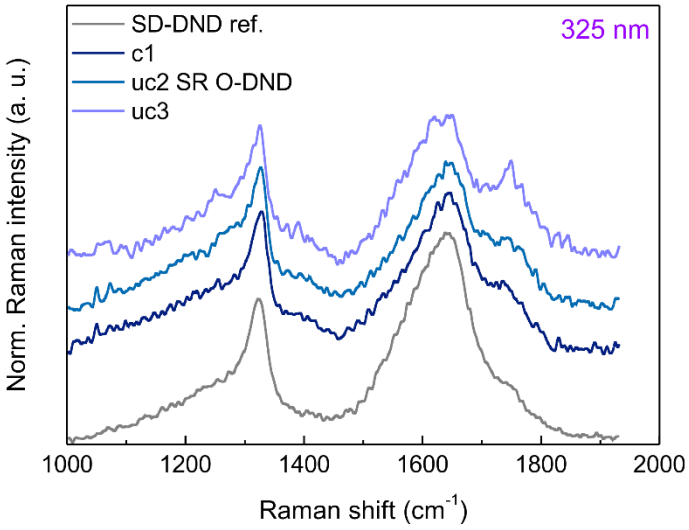

Figure 7. Raman spectra of the SD-DND ref., c1, uc2, uc3 fractions of the SR O-DNDs obtained with 325 nm excitation.

Focusing on the diamond T_2g mode line profile, the diamond line shapes of the HPHT O-NDs fractions obtained with the 785 nm excitation are shown in detail in Figure 8. Here, the 785 nm excitation wavelength, the lowest available photon energy, was used to minimize thermal effects. The spectra of HPHT O-NDs fractions are compared to the reference Ib diamond single crystal. The small residual "D" band component at about 1320 cm^{-1} is far enough from the main diamond line to be fitted appropriately, or omitted the in case of c1 fraction. For the three size fractions, it is observed that the diamond line shifts are only minor, always lower than ca 1 cm^{-1}. The same trends were obtained using the 514 nm excitation (not shown). In both cases, thermally-induced frequency downshifts were minimized when the power density at the sample was well below ca 1 $mW/\mu m^2$. Line broadening is moderate, always in the 8-13 cm^{-1} range,

much lower than 30 cm^{-1} usually observed for DND samples, and allows some discrimination between the centrifuged and ultracentrifuged fractions. In contrast, UV excitation (325 nm) already induces noticeable diamond line shift and broadening also to the HPHT O-NDs spectra. Fig. 8e clearly shows that despite the precautions taken, i.e. a power density close to 700 $\mu W/\mu m^2$, heating under the focused 325 nm laser seems unavoidable when the analysis is conducted in a point illumination mode. The line shifts are then more pronounced with decreasing particle size and can reach values as high as 2 - 5 cm^{-1}, hence showing that the analysis is conducted in approx. 120 °C - 300 °C range. Again, for each HPHT O-ND fraction, line broadening is still moderate, and much lower than the one observed for the SD-DND reference sample (see the grey trace in Figure 8e).

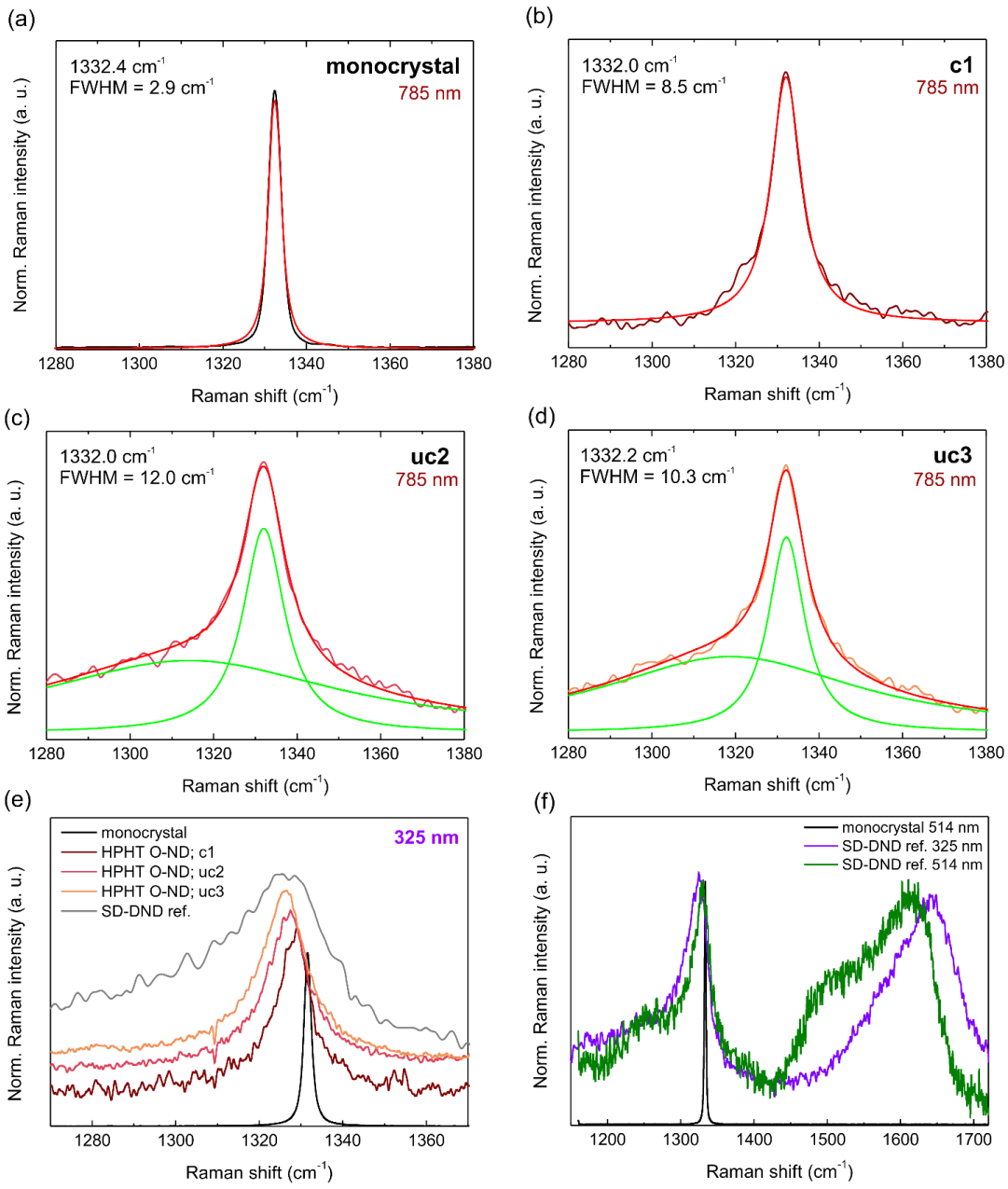

Figure 8. High-resolution Raman spectra of the monocrystalline diamond (a) and HPHT O-NDs c1 (b), uc2 (c), uc3 (d) fractions obtained by 785 nm excitation, including Lorentzian fits. Comparison of the Raman spectra of the monocrystalline diamond and HPHT O-NDs c1, uc2, uc3 fractions and the 5 nm SD-DND ref. obtained by 325 nm excitation (e). Raman spectra of

the SD-DND ref. sample obtained by 325 nm (purple) and 514 nm (green) excitation with minimized temperature effect by line excitation (f).

The high-resolution analysis of the SR O-DND fractions by 785 nm and/or 514 nm excitation was not possible within the exception of the SD-DND reference. For this particular SD-DND reference, we compare in Figure 8f spectra obtained with 514 nm and 325 nm excitations, using high resolution conditions. In both cases, the power density at the sample was much lower than 1 $mW/\mu m^2$. In spite of the low laser power a characteristically strong line downshift (≈ 1325 cm^{-1}) and significant broadening (FWHM ≈ 39 cm^{-1}) is observed with 325 nm excitation. By contrast, significantly smaller downshift (≈ 1329 cm^{-1}) and broadening (FWHM = 29 cm^{-1}) was observed with the 514 nm using line excitation. This clearly evidences sample heating under 325 nm laser and, in our opinion, clearly underlines the difficulty of undertaking this type of analysis in a reliable way. When thermal effects are minimized by using line excitation, the line shift and broadening, characteristic to DNDs, is significantly reduced (3-4 cm^{-1}, 29 cm^{-1}, respectively) to values much lower than those commonly reported in the literature [12,15,17–21,73,74] and much closer to those observed for HPHT O-NDs. Yet, despite the volumetric mode particle size of HPHT O-ND uc3 fraction (see Figure 1 and Table 1) being already well below a typical DND size, its Raman spectrum still looks very different from the DND spectrum.

The last spectral region examined in this study involved the close vicinity to the Rayleigh line employing the Bragg rejection filters. Here, analogically to the Raman confined optical modes, low-frequency modes were expected for such small particles. Such modes may be described as acoustic vibrations localized in small particles with a size of a few nanometers. These modes are not to be confused with Brillouin modes, even though they are usually observed at low to very low frequencies, below ca 50 cm^{-1} for most semiconducting or even metallic

materials. Interestingly, as we will see, the frequency of these modes is expected to inversely scale with the particle diameter. Thus, the observation of these modes would be another convenient way to determine a mean particle size. Because the frequencies of such modes are related to the sound velocity, which is much higher in diamond than in other materials, these modes are expected at relatively high frequencies. Hence they should be *a priori* easier to detect than in other materials as one can work further from the Rayleigh line. Note also that *ab initio* simulations predict ND "breathing"-like modes, with similar characteristic frequencies [75]. Yet, to our knowledge, these modes have never been experimentally confirmed or even sought after in NDs.

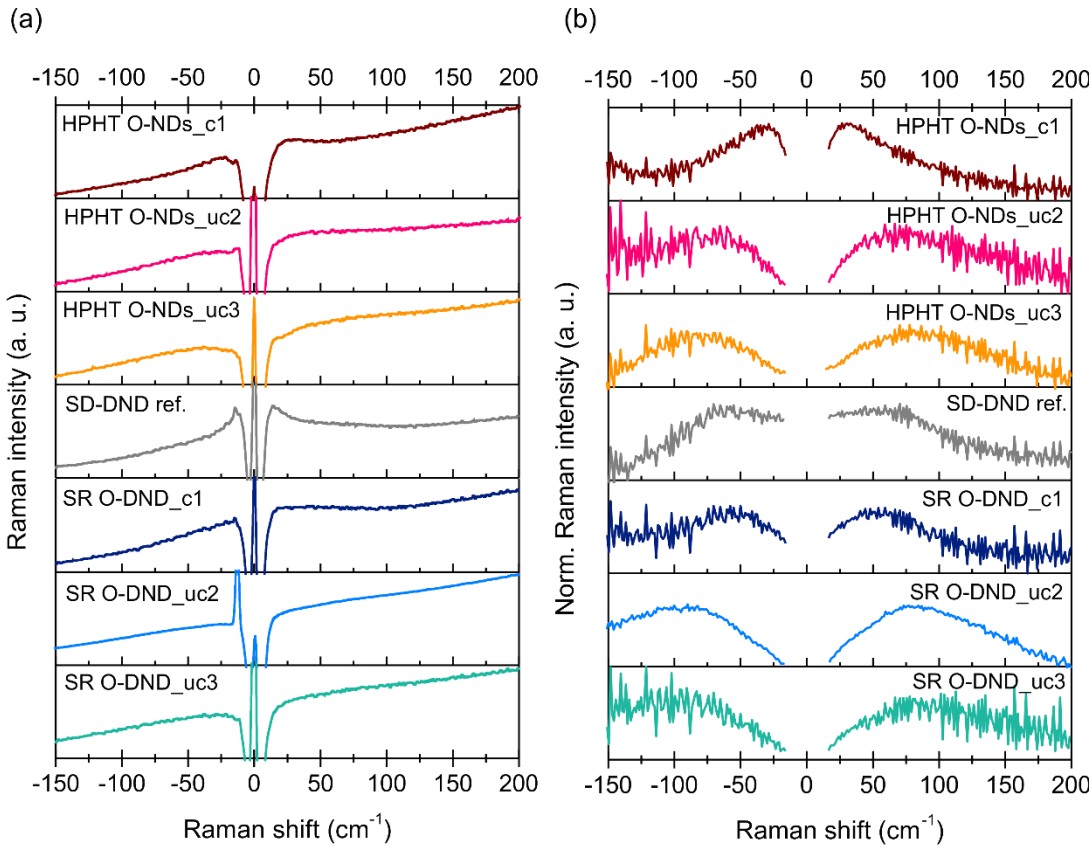

Figure 9. Low-frequency Raman signals of c1, uc2 and uc3 fractions of HPHT O-NDs and SR O-DNDs and of the SD-DND reference. Raw data (a), after baseline subtraction and temperature correction (b).

Here, scattering at low frequencies has effectively been detected as shown in the Figure 9a using a 514 nm excitation. Very similar low frequency scattering was also observed using a 532 nm excitation and a different spectrometer, the raw data of HPHT O-NDs are shown in the Figure S7. In all cases, it was necessary to increase the incident power density to a few $mW/\mu m^2$ to detect them clearly. These weak signals were detected on both sides of the Rayleigh line. This is the first indication that they are not due to PL. Once corrected from the Bose population factor (n and n+1 for the Anti-Stokes and Stokes sides respectively), these signals should be perfectly symmetrical in intensity. Thus, to extract more reliable information from these data, the raw spectra were first corrected for the PL backgrounds. Second, the resulting signals were divided by the Bose statistics population factor to get the corresponding temperature-corrected signals. In this correction, the temperature was the only adjustable parameter which was used to make the two signals symmetrical. Such a correction effectively allowed to get symmetrical bands, see Figure 9b. This is a second confirmation that these low frequency signals are indeed due to Raman scattering. Interestingly, the Bose correction consistently gave temperatures in the 150-250 °C range for both HPHT O-ND and SR O-DND sample sets, with slightly higher values for DNDs. In the case of HPHT O-NDs, these temperatures matched those obtained from the downshift of the first-order diamond Raman line, assuming no strong confinement-induced downshift. Thus, even though the intensity of these signals is low and the correction for the PL background can be problematic, the discussion of these signals in terms of acoustic modes localized in small particles seems reasonable.

The Raman spectroscopy correlated with other methods including careful PSD analysis thus showed: 1) experimental issues such as heating and PL interference patterns which may distort the obtained results, 2) way to minimize such effects, 3) fundamental differences between sub-5 nm DND and HPHT NDs, and 4) the first experimental evidence of size-sensitive acoustic breathing modes in NDs.

Discussion

Size-dependent nanodiamond purity and crystallinity

The annealing in air was employed for removing the non-diamond sp^2-C from the ND surface [12,71] as well as for controlled size reduction of DNDs [23,24]. From a chemical viewpoint, such purification effect was obvious in the case of HPHT NDs as the XPS and Raman spectroscopy confirmed a low residual graphitic carbon content compared to original material. This low content is preserved down to the sub-5 nm size region. In that sense our results complement well the previous microscopic study showing nearly complete removal of non-diamond carbon from HPHT NDs resulting in a very sharp interface between the diamond crystal lattice surface and the outer environment [58] as suggested also theoretically[76]. Yet, the location and form of the residual non-diamond carbon as well as the detailed surface structure of the HPHT O-NDs remain to be elucidated.

The situation is different for SR O-DNDs. The sp^2 content seems rather insensitive to size reduction, an indication that some of the sp^2 defects may be located in the volume of the particles[47]. Still, according to XPS, the sp^2/sp^3 bond ratio increased with decreasing particle size

for all samples indicating some presence of a surface sp^2 carbon on both types of NDs. This agrees with the previous finding reported for DNDs[77–79].

From a structural point of view, our results show that both oxidized HPHT ND and DND nanoparticles are stable down to ultra-small sizes, below 3 nm. However, they are structurally different, and the differences are preserved down to the sub-5 nm region as no convergence e.g. in the Raman spectra was observed. Such strong difference in crystallinity and sp^2 carbon purity retained between the two types of NDs on similar size scale down to several nanometers rules out a possibility that the O-DND defective and/or a core-shell structure is only a consequence of their ~ 5 nm size. These features thus must arise from the detonation synthesis.

In HPHT O-NDs, both XRD and Raman spectroscopy were sensitive to size reduction through some evolution, at least a broadening of their characteristic signals. In contrast, XRD and Raman spectroscopy showed themselves insensitive to O-DND size decrease. In particular, Raman line profiles (Figure 7) remain constant for all the SR O-DND fractions examined. In DNDs, the effects of particle size reduction are thus very small, if any. The Raman line profile of the DND samples is thus controlled by the high defect density within each particle, but not by its apparent size. Indeed, all TEM studies have shown that twins and stacking faults are present in a large amount within the core of the DND particles[71].

Another Raman spectral feature makes it possible to differentiate both types of NDs, as shown in Figure 5. In the case of DNDs, the Raman first-order mode is clearly superimposed on a broader line, peaking at about 1250 cm^{-1}. This broad line is clearly accompanied with a continuous signal with another apparent maximum at about 700 cm^{-1}. A similar continuous signal may was detected for HPHT O-NDs even though it is much weaker in intensity. As can be

seen in Figure 5, this signal closely resembles the diamond VDOS, in particular when plotted as a reduced Raman spectrum, with thermal occupation effects removed from the signal. Generally speaking, the observation of this type of signal suggests the presence of very disordered or even amorphous materials, for which the translational symmetry does not extend beyond 3 or 4 interatomic distances. Such features can be correlated with domains having very small coherence lengths, either in the form of a disordered surface shell, as already suggested by other techniques [80–82], or simply in the form of isolated and highly twinned or defective crystals. In analogy, it is not unusual to detect amorphous-like silicon material when analyzing silicon nanoparticles [83] or thin silicon films prepared by chemical vapor deposition [84]. This signal is hardly detectable for the HPHT O-NDs, which, once again, confirms their better crystallinity compared to DNDs. From this point of view the DND structure can be described as highly defective diamond crystal lattice in which the high concentration of defects causes the mean effective coherence length to be not more than 2-3 nm, i.e. lower than the typical particle size.

Confined optical mode: temperature vs. confinement effects in NDs

For both kinds of oxidized NDs (HPHT or detonation) and all the size fractions down to 2-3 nm, Raman spectra could be obtained. Yet, our results clearly show that getting Raman spectra of such small NDs needs some particular care. Some of the issues are already known and often mentioned in the literature, namely high PL backgrounds and uncontrolled sample heating. However, our results reveal that it is mandatory to use unusually low power densities, as a rule much lower than 1 $mW/\mu m^2$ in the visible range. In the UV range, spectra could only be obtained reliably with power densities as low as few tens of $\mu W/\mu m^2$. Sample heating was mentioned for

larger HPHT NDs [19] but has rarely been discussed for much smaller DNDs. Only after minimization of the temperature effect, reliable diamond Raman line profiles characteristics of nanodiamonds were obtained. Moreover, even for the lowest power densities, sample instability under the focused laser beam (UV to visible) is still an issue that will be discussed in a forthcoming paper. This instability was reflected by pronounced evolution of the diamond and sp^2 carbon-related Raman features as well as noticeable evolution of the PL background as a function of illumination time. These effects were in our case minimized by using line instead of point illumination during the Raman measurements.

Appearance of confined optical and acoustical modes is one of the features expected for sub-10 nm NDs. Both kinds of modes were effectively observed for other non-polar, group IV semiconducting materials, i.e. silicon and germanium. The optical mode confinement is in most cases described by the so-called phonon confinement models (PCM) or equivalently by the so-called spatial correlation model. For most semiconducting materials, when the particle size is reduced down to a few nanometers, peak position shifts, peak broadening, and asymmetries of optical phonon bands appear. Because of the usual downwards dispersion of the optical modes, Raman peaks gets progressively broader and asymmetric on their low energy side as the particle size decreases. This effect has been used to determine a particle size, or more exactly a coherence length in various nanomaterials. This effect has also been frequently used to explain the downshift and broadening of the diamond optical mode regularly observed for DNDs[8,15–22].

When considering the size distributions and the Raman spectra measured in this work, it leads us to conclusion that most of the PCM models published so far overestimate the line shifts induced by the localization of vibrations in the volume of the diamond nanocrystal. Yet, after suppression of possible thermal effects, appropriate PCM models seem to provide correct

estimations for silicon nanocrystals, for example predicting downshifts of about 3.5 cm^{-1} for nanoparticles with a 3 nm diameter[83]. In the following part, we will keep in mind this order of magnitude. Without giving all the details of the calculations, (for such a purpose, see for example Refs. [85,86]), it is useful to recall here the main assumptions of the PCM model. Phonon confinement models aims at describing vibrations in materials at the nanoscale as localized (i.e. confined) phonons of the parent bulk crystals. For crystals, for which translational symmetry is preserved over large dimensions, vibrational modes (i.e. the phonon wave functions) are described in terms of plane waves. These plane waves have an infinite extension. The energies of crystalline vibrations probed by Raman spectroscopy are usually lower than 250 meV (about 2000 cm^{-1}), and those of the exciting visible laser light are about 1.5 – 5 eV. Therefore, we get $\omega_s \approx \omega_i$ (subscripts *s* and *i* stand for scattered and incident, respectively) and the wavevector in a typical backscattering experiment will be on the order of $q \approx 4\pi n/\lambda$, much smaller than the wavevector $q = 2\pi/a$ at the boundary of the Brillouin zone, where *a* is the lattice constant, *n* denotes the refractive index of the sample, and λ is the excitation wavelength. Therefore, for Raman scattering, this selection rule implies the contributions of phonons close to the center of the Brillouin zone (Γ point). This is known as the $q \approx 0$ selection rule.

When vibrations are restricted within very small particles or crystalline domains, bulk planewave-like phonon wavefunctions cannot exist anymore. Thus, phonons can no longer be described in terms of plane waves. They are rather described as "wave packets" with spatial dimensions similar to the crystallite size. Therefore, phonons out of an interval of q wavevectors centered around $q = 0$ may contribute to the Raman spectra. An uncertainty in wavevector $\Delta q \approx 1/L$ is thus introduced, which will be larger for smaller particle sizes *L* because the "wave packet" becomes more localized in real space. Since the phonon dispersion curves are in general

not flat, new frequencies will be introduced in the Raman spectra when contributions from phonons having significantly different wave vectors start playing a role. Therefore, the confined phonon is composed of a sum of bulk-like phonons with a range of wavevectors around the Brillouin zone center. When the size of perfect crystal (or coherence length) is close to a few interatomic distances, the whole Brillouin zone is probed and the Raman spectrum reflects the VDOS. Spectra of amorphous solids (systems with the smallest coherence lengths) effectively mimic the VDOS. This is what was observed and discussed above for DNDs.

In the PCM model, phonon localization is simply imposed by a weighting $W(r, L)$ function which restricts the vibration inside the particle. This function is not a known function *a priori*. Gaussian or sinc functions are usually used to describe the phonon confinement, without any physical justifications. This is one of the reasons why the PCM model is usually considered as purely phenomenological. Another prerequisite is to find a right description of the phonon dispersion curves. For such a purpose, different approaches have been used, in most cases by using a simple one-dimensional linear-chain model or by weighting the Δ, Σ, and Λ branches according to their relative degeneracy. Thus, averaged 1D dispersion curve are usually introduced, typically in the form $\omega(q) = A + Bcos(\pi q)$ as suggested by 1D linear chain models. Other strategies have been used in the case of silicon [83]. Such strategies work well because the LO and TO branches are relatively similar in the high symmetry directions of the Brillouin zone. Such an approach may be problematic in the case of diamond.

One of the unusual properties of diamond is the upward curvature, or overbending, of the LO phonon dispersion away from the Γ point. Such overbending has been predicted by *ab initio* calculations [87,88]. It was also measured and quantified using inelastic neutron and X-ray

scattering [89]. These data clearly revealed the overbending for $0.15 < q < 0.25$, here in $2\pi/a$ units. The maximum of the overbending was determined to be 1.5 meV (12 cm^{-1}), 0.5 meV (4 cm^{-1}), and 0.2 meV (1.6 cm^{-1}), along the Γ-X, Γ-L, and Γ-K directions, respectively. This overbending is evidenced as a sharp peak at about 1336 cm^{-1} in the diamond VDOS, i.e. about 4 cm^{-1} above the zone-center frequency. It is also reflected as a sharp peak in the diamond Raman second-order spectrum at twice this frequency. This overbending is probably hard to reproduce using 1D averaged phonon dispersion curves. Therefore, more physically consistent models aim to adopt a 3D integration all over the *q*-space, which requires the exact knowledge of the phonon dispersion at any arbitrary q-point [20–22]. However, to date, all these models still predict a downshift of the diamond T_{2g} modes for coherent lengths lower than ca 20 nm. Another characteristic feature of diamond is its small lattice parameter, much smaller than in silicon. According to the PCM model, a direct consequence is that a smaller region of the Brillouin zone will be probed for diamond for a given coherence length.

Thus, in this simple intuitive way, these few diamond-specific characteristics may explain why it may not be surprising to observe rather small line shifts, if any, for particle sizes (or coherence lengths) of few nanometers. It may be explained in part by a combination of the small diamond lattice parameter together with the upward curvature, or overbending, of the LO phonon dispersion away from the Γ point which can nullify the down shift of the diamond Raman line with decreasing size. In such case, the difference between detonation and HPHT NDs is likely explained by the much higher defect density in DNDs leading to much lower coherence lengths that do not correspond to the apparent particle size. Note that a particle size of about 3 nm, i.e. the mean value of the uc3 fractions in this work, correspond to 8 or 9 lattice parameters. Such particles contain less than 3000 atoms. Nevertheless, in the case of SR-ONDs,

Raman spectroscopy does not clearly distinguish them from larger DND particles, as judged from the unshifted frequency of its first-order Raman mode.

The PCM model also completely ignores macro- and micro-strain effects. However, the available XRD data [12,45] as well as the XRD data in this study tend to indicate that tensile strain is present in DNDs. As such, it can also contribute to the higher line downshifts observed for DNDs. Possible thermal effects, i.e. uncontrolled sample heating is another issue, as we have shown. In our opinion, the use of the phonon confinement models for nanodiamonds, even in a qualitative way, should therefore be considered with a great care.

Confined acoustic modes

A size dependent, low-frequency scattering in NDs was observed for all the examined samples of HPHT and detonation NDs. For diamond, such low-frequency vibration modes were predicted by molecular mechanics force field calculations, see for example Ref. [75]. In such case, the nanocrystal may be described as a big molecule, and normal mode frequencies are determined through the diagonalization of the dynamical matrix. The most intense peak in the low frequency region is produced by a fully symmetric "breathing" mode of the whole particle. In another approach, for nanoparticles whose sizes is below ca 10 nm, such modes are also described in terms of Lamb's modes, i.e., in their simplest formulation, as the vibrational modes of an isotropic elastic sphere under stress-free boundary conditions. Here, the nanoparticle is considered as a continuous medium with known isotropic elastic properties. The eigen-modes and the eigen-frequencies of vibration are obtained by solving the Navier equation. A complete description of these vibrational modes falls completely outside the scope of the present paper, this information may be found in Refs. [90–92] and references therein. Summarizing, Lamb's modes

are classified into spheroidal (breathing and twisting motion) and torsional (twisting motion only) modes. Each frequency $\omega_{n,l}$ depends on the branch index n and angular momentum l, according to:

$$\omega_{n,l} = S_{n,l}\frac{v_t}{cL}$$

where v_t is the transverse sound velocity, c the light velocity and L the particle radius; $S_{n,l}$ is a factor depending on the mode *(n, l)* under consideration. The frequencies of torsional modes depend only on the transverse sound velocity, whereas those of spheroidal modes depend on the ratio of the longitudinal and transverse sound velocities. For such description, far from resonance excitations, Duval and co-workers [93] have shown on the basis of symmetry arguments that the only Raman-active modes of a sphere are the symmetric $l = 0$ and quadrupolar $l = 2$ spheroidal modes. The former produce polarized spectra and the latter depolarized spectra. The $l = 0$ spheroidal modes is purely radial with complete spherical symmetry and can be viewed as a particle breathing mode.

At first, we considered the so-called Lamb's model and used the simplest spherical particle approximation. We used the calculation routine given in [94], which allows both the calculation and the visualization of the vibration modes of a free homogeneous sphere, assuming isotropic elasticity. Sound velocities and particle sizes are required as input. We considered the following limiting values: (i) the longitudinal and transverse sound velocities of diamond single crystal along the <100> direction [85], and (ii), the average longitudinal and transverse sound velocities estimated from a Voigt-Reuss-Hill averaging procedure. In the second approach, Young's modulus, and Poisson's ratio of single-crystal diamonds were estimated by averaging the elastic compliance and stiffness coefficients for all the crystal orientations. The complete

averaging protocol may be found in Refs. [95,96]. Sound velocities were then computed from the averaged Young's modulus and Poisson ratio. For computation of the Raman-allowed symmetric and quadrupolar spheroidal modes, we used the averaged sound velocities values, giving 18140 and 12330 ms^{-1} for V_l and V_t respectively. Both approaches consistently gave the same trends as shown in Fig. 10.

For comparison, we also used some of the results provided by the molecular-like approach described in Ref. [75]. In this work, calculations were carried out both for particles of octahedral and tetrahedral shapes. They revealed that the most intense response in the low frequency region for small diamond nanocrystals in the 0.5 – 3 nm range is produced by the fully symmetric breathing mode of the particles. The frequency of this fully symmetric breathing mode was observed to be approximately the same for octahedral and tetrahedral shapes built with the same number of carbon-carbon bonds. Because such *ab initio* calculations cover only a very small particle diameter range, we have extrapolated this data set to larger particle sizes, still assuming that frequencies are inversely proportional to the particle diameters. Such data set shows that this assumption seems realistic for small particle sizes. Fig. 10 shows that both approaches result in the same trends for particle sizes in the 1 – 3 nm range, even though the *ab initio* method tends to indicate slightly higher frequencies. The extrapolation of the *ab initio* calculations towards higher particle sizes also nicely corresponds to those determined from the Lamb's model. Thus, both approaches suggest observable frequencies in the 200-20 cm^{-1} range for the particle sizes in the 2 – 20 nm range.

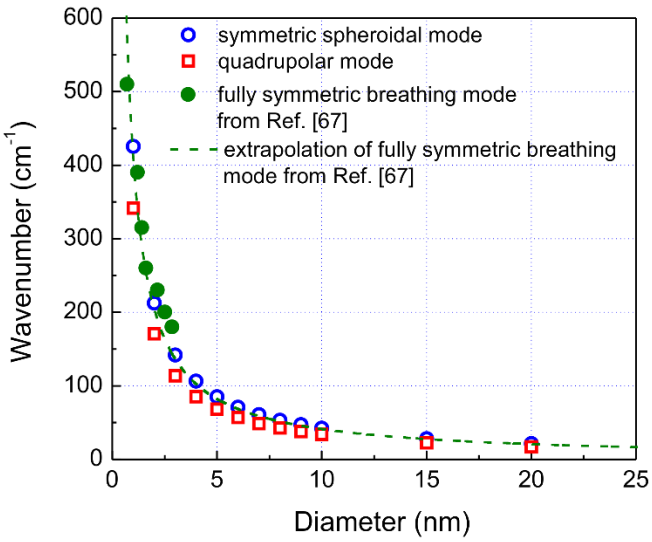

Figure 10. Variation in the estimated Raman shifts of low frequency modes with particle size according to the Lamb's model and the ab initio approach of Ref [75]. Open blue circles: symmetric spheroidal mode. Open red squares: quadrupolar mode. Full green circles: fully symmetric breathing mode from Ref [75]. Dashed green line: extrapolation of the fully symmetric breathing mode to higher particle sizes assuming that frequencies are inversely proportional to the particle diameters.

Because the observed low frequency scattering falls in the expected frequency range, it can be interpreted as confined vibration modes in NDs: (i) it is sample and size dependent, (ii) for both HPHT O-ND and SR O-DND there is a shift of the maxima to higher wavenumbers in agreement with the decreasing ND size from c1 to uc3 fraction. The observed maxima evolve in the 30 - 80 cm^{-1} range, roughly corresponding to particle sizes in the 12 – 5 nm range. These modes may thus provide a rather sensitive way to estimate the ND PSD below 10 nm by using Raman spectroscopy.

The mean values of the PSD may be slightly overestimated though. First, the sound velocity for single crystal diamond may be not completely adequate for defective nanoparticles, DND in particular. The use of lower sound velocity resulted in the mean particle size closer to the PSD maxima observed by other techniques in this work (see Figure 1 and Table 1). Second, as already mentioned, the HPHT O-NDs have highly irregular shapes, largely deviating from the sphere approximation used for the Lamb's model or the regular crystal shapes used in Ref [75]. Moreover, diamond mechanical properties are known to be strongly anisotropic. Diamond at the nanometric scale can only be produced by very energetic techniques, here, detonation or grinding. This makes the control of the particle shape difficult which, in turn, complicates the application of models. Finally, the PSD range certainly plays a role. From technological viewpoints, the PSDs seem rather narrow. However, from a spectroscopic point of view, it remains rather large (close to a factor of 3-4). The expected mode frequencies are supposed to vary rapidly in the considered size range, which can perhaps explain the rather large width of the low frequency scattering. Finally, also other light scattering mechanisms or effects can contribute to these signals, for example electronic Raman scattering or incompletely rejected elastic scattering tail.

Conclusions

We investigated structure and surface chemistry as well as compared the HPHT and detonation NDs at the sub-5 nm size scale where confinement phenomena are expected. Ultracentrifugation was used to get three size fractions of HPTH O-NDs and SR O-DNDs whose size distribution was analyzed by combining DLS, SAXS, AUC, XRD and TEM methods. Such

a comprehensive analysis using complementary methods was shown necessary to retrieve reliable mass/volume-weighted PSD data that are crucial for the interpretation of subsequent spectroscopic and structural size-dependent properties. The analysis revealed similar PSD of the finest uc3 fractions with mode sizes down to the 2-3 nm range for both HPHT O-NDs and SR O-DNDs. This enabled a detailed comparison of HPHT O-NDs with SR O-DNDs in the sub-5 nm region and some discrimination between the effects of size and structural defects on their spectroscopic response.

XPS, XRD and Raman spectroscopy confirmed that a major fraction of the HPHT O-NDs and SR O-DND down to 2-3 nm remains in a diamond phase. All these methods also clearly showed that the HPHT NDs and DNDs are structurally strongly different and that these differences are preserved down to the sub-5 nm particle size range. The analysis further showed that HPHT O-NDs can be prepared with only a minor content of sp^2, graphitic carbon, which is interesting from an application point of view. FTIR spectroscopy revealed a surface chemistry evolution with decreasing size in both HPHT O-NDs and SR O-DNDs as well as noticeable differences between the surface chemistry and nitrogen content in the HPHT O-NDs and SR O-DNDs.

The availability of NDs of different origins in the sub-10 nm range allowed to revisit some of the expected size effects, or so-called confinement effects, on the line shape of the Raman diamond optical mode of T_{2g} symmetry. From a methodological point of view, unusually low excitation laser power densities had to be used to minimize thermally induced line shifts. Interestingly, NIR and visible excitations could be used for HPHT O-NDs, which further contributed to lower the unwanted thermal effects. In that particular case, we evidenced nearly constant diamond line position (within 1 cm^{-1}) accompanied by a noticeable broadening (up to 12

cm^{-1}) while decreasing ND mode size down to ~ 3 nm. On the other hand, XPS (C1s peak), XRD (111 diffraction) and Raman spectroscopy (T_{2g} mode) showed insensitivity to size reduction for SR O-DNDs. In both cases, the size insensitivity seems to rule out any direct use of the current phonon confinement models for NDs, even in a qualitative way. This is also a strong indication that the Raman line profile for DNDs is controlled by the high defect densities within each particle, and not by its apparent size. Some of the possible limitations of the phonon confinement models were discussed accordingly.

Moreover, we detected size-dependent low-frequency scattering for all NDs. This scattering was systematically observed in the 20 – 200 cm^{-1} range for all the samples examined in this work. Such a low frequency scattering is expected to be observed in sub-10 nm nanoparticles in general, in a frequency range that depends on their mechanical properties. Two different theoretical models were considered to estimate the frequencies as function of the particle size. The size dependence for both HPHT NDs and DNDs low frequency scattering suggests that they might correspond to confined acoustic vibrational, "breathing-like" modes. The low-frequency Raman scattering may thus provide another way for size distribution analysis of nanodiamonds.

ASSOCIATED CONTENT

Supporting Information. Diffraction patterns of the SD-DND-reference, SR O-DND c1, uc2, uc3 fractions and of the HPHT O-ND c1, uc2, uc3 fractions (Figure S1). Description of the model to fit the SAXS data, raw SAXS data of the SD DND reference, the three fractions of the HPHT O-NDs, and two measureable fractions of the SR O-DNDs (Figure S2). SAXS data with

subtracted background, and the fits of HPHT O-NDs for the c1, uc2 uc3 fractions, SD DND ref, and SR O-DNDs c1 and uc2 fractions (Figure S3). SAXS data and size distribution fit of the SR O-DND c1 using a model involving spheres and discs (Figure S4). Multiwavelength Raman spectra of the three fraction of the second HPHT O-NDs sample set having more sp^2-C (Figure S5). Raman spectra of the SD-DND reference and three fraction of the SR O-DNDs acquired with 442 nm excitation (Figure S6). Broad range Raman spectra of the HPHT O-NDs c1, uc2 and uc3 fractions obtained with 532 nm excitation using Bragg rejection filters (Figure S7). This material is available free of charge via the Internet at http://pubs.acs.org.

AUTHOR INFORMATION

Corresponding Author

*Stepan Stehlik, stehlik@fzu.cz

Author Contributions

The manuscript was written through contributions of all authors. All authors have given approval to the final version of the manuscript.

ACKNOWLEDGMENT

This study was supported by the Czech Science Foundation (GACR) grant number 18-11711Y and by the Ministry of Education, Youth and Sports of the Czech Republic (MEYS) under the project CZ.02.1.01/0.0/0.0/16_019/0000760 (Solid21) and the project CZ.02.1.01/0.0/0.0/16_019/0000778 (CAAS). We also acknowledge use of the CzechNanoLab research infrastructure supported by the MEYS (LM2018110). P. Bauerova and J. Libertinova are acknowledged for their help in preparation of samples as well as for the TEM work. E.

Shagieva is acknowledged for her help in FTIR measurements. The authors would also like to thank B. Sochor for the helpful suggestions and discussions regarding the SAXS analysis.

REFERENCES

(1) Mochalin, V. N.; Shenderova, O.; Ho, D.; Gogotsi, Y. The Properties and Applications of Nanodiamonds. *Nature Nanotechnology* **2011**, *7* (1), 11–23. https://doi.org/10.1038/nnano.2011.209.

(2) Torelli, M. D.; Nunn, N. A.; Shenderova, O. A. A Perspective on Fluorescent Nanodiamond Bioimaging. *Small* **2019**, 1902151. https://doi.org/10.1002/smll.201902151.

(3) Nunn, N.; Torelli, M.; McGuire, G.; Shenderova, O. Nanodiamond: A High Impact Nanomaterial. *Current Opinion in Solid State and Materials Science* **2017**, *21* (1), 1–9. https://doi.org/10.1016/j.cossms.2016.06.008.

(4) Krueger, A.; Lang, D. Functionality Is Key: Recent Progress in the Surface Modification of Nanodiamond. *Advanced Functional Materials* **2012**, *22* (5), 890–906. https://doi.org/10.1002/adfm.201102670.

(5) Merz, V.; Lenhart, J.; Vonhausen, Y.; Ortiz-Soto, M. E.; Seibel, J.; Krueger, A. Zwitterion-Functionalized Detonation Nanodiamond with Superior Protein Repulsion and Colloidal Stability in Physiological Media. *Small* **2019**, 1901551. https://doi.org/10.1002/smll.201901551.

(6) Gibson, N.; Shenderova, O.; Luo, T. J. M.; Moseenkov, S.; Bondar, V.; Puzyr, A.; Purtov, K.; Fitzgerald, Z.; Brenner, D. W. Colloidal Stability of Modified Nanodiamond Particles. *Diamond and Related Materials* **2009**, *18* (4), 620–626. https://doi.org/10.1016/j.diamond.2008.10.049.

(7) Williams, O. A.; Hees, J.; Dieker, C.; Jäger, W.; Kirste, L.; Nebel, C. E. Size-Dependent Reactivity of Diamond Nanoparticles. *ACS Nano* **2010**, *4* (8), 4824–4830. https://doi.org/10.1021/nn100748k.

(8) Mykhaylyk, O. O.; Solonin, Y. M.; Batchelder, D. N.; Brydson, R. Transformation of Nanodiamond into Carbon Onions: A Comparative Study by High-Resolution Transmission Electron Microscopy, Electron Energy-Loss Spectroscopy, x-Ray Diffraction, Small-Angle x-Ray Scattering, and Ultraviolet Raman Spectroscopy. *Journal of Applied Physics* **2005**, *97* (7), 074302. https://doi.org/10.1063/1.1868054.

(9) Stehlik, S.; Petit, T.; Girard, H. A.; Arnault, J.-C.; Kromka, A.; Rezek, B. Nanoparticles Assume Electrical Potential According to Substrate, Size, and Surface Termination. *Langmuir* **2013**, *29* (5), 1634–1641. https://doi.org/10.1021/la304472w.

(10) Stehlik, S.; Glatzel, T.; Pichot, V.; Pawlak, R.; Meyer, E.; Spitzer, D.; Rezek, B. Water Interaction with Hydrogenated and Oxidized Detonation Nanodiamonds — Microscopic and Spectroscopic Analyses. *Diamond and Related Materials* **2015**. https://doi.org/10.1016/j.diamond.2015.08.016.

(11) Rehor, I.; Cigler, P. Precise Estimation of HPHT Nanodiamond Size Distribution Based on Transmission Electron Microscopy Image Analysis. *Diamond and Related Materials* **2014**, *46*, 21–24. https://doi.org/10.1016/j.diamond.2014.04.002.

(12) Stehlik, S.; Varga, M.; Ledinsky, M.; Jirasek, V.; Artemenko, A.; Kozak, H.; Ondic, L.; Skakalova, V.; Argentero, G.; Pennycook, T.; Meyer, J. C.; Fejfar, A.; Kromka, A.; Rezek, B. Size and Purity Control of HPHT Nanodiamonds down to 1 Nm. *The Journal of Physical Chemistry C* **2015**, 150825003821009. https://doi.org/10.1021/acs.jpcc.5b05259.

(13) Boudou, J.-P.; Tisler, J.; Reuter, R.; Thorel, A.; Curmi, P. A.; Jelezko, F.; Wrachtrup, J. Fluorescent Nanodiamonds Derived from HPHT with a Size of Less than 10nm. *Diamond and Related Materials* **2013**, *37*, 80–86. https://doi.org/10.1016/j.diamond.2013.05.006.

(14) Nunn, N.; Shenderova, O. Toward a Golden Standard in Single Digit Detonation Nanodiamond: Toward a Golden Standard in Single Digit Detonation Nanodiamond. *physica status solidi (a)* **2016**, *213* (8), 2138–2145. https://doi.org/10.1002/pssa.201600224.
(15) Mermoux, M.; Chang, S.; Girard, H. A.; Arnault, J.-C. Raman Spectroscopy Study of Detonation Nanodiamond. *Diamond and Related Materials* **2018**, *87*, 248–260. https://doi.org/10.1016/j.diamond.2018.06.001.
(16) Ager, J. W.; Veirs, D. K.; Rosenblatt, G. M. Spatially Resolved Raman Studies of Diamond Films Grown by Chemical Vapor Deposition. *Phys. Rev. B* **1991**, *43* (8), 6491–6499. https://doi.org/10.1103/PhysRevB.43.6491.
(17) Yoshikawa, M.; Mori, Y.; Obata, H.; Maegawa, M.; Katagiri, G.; Ishida, H.; Ishitani, A. Raman Scattering from Nanometer-Sized Diamond. *Applied Physics Letters* **1995**, *67* (5), 694. https://doi.org/10.1063/1.115206.
(18) Osswald, S.; Mochalin, V. N.; Havel, M.; Yushin, G.; Gogotsi, Y. Phonon Confinement Effects in the Raman Spectrum of Nanodiamond. *Physical Review B* **2009**, *80* (7). https://doi.org/10.1103/PhysRevB.80.075419.
(19) Chaigneau, M.; Picardi, G.; Girard, H. A.; Arnault, J.-C.; Ossikovski, R. Laser Heating versus Phonon Confinement Effect in the Raman Spectra of Diamond Nanoparticles. *Journal of Nanoparticle Research* **2012**, *14* (6). https://doi.org/10.1007/s11051-012-0955-9.
(20) Korepanov, V. I.; Witek, H.; Okajima, H.; Ōsawa, E.; Hamaguchi, H. Communication: Three-Dimensional Model for Phonon Confinement in Small Particles: Quantitative Bandshape Analysis of Size-Dependent Raman Spectra of Nanodiamonds. *The Journal of Chemical Physics* **2014**, *140* (4), 041107. https://doi.org/10.1063/1.4864120.
(21) Korepanov, V. I.; Hamaguchi, H. Quantum-Chemical Perspective of Nanoscale Raman Spectroscopy with the Three-Dimensional Phonon Confinement Model: Quantum-Chemical Perspective of Nanoscale Raman Spectroscopy. *J. Raman Spectrosc.* **2017**, *48* (6), 842–846. https://doi.org/10.1002/jrs.5132.
(22) Korepanov, V. I. Localized Phonons in Raman Spectra of Nanoparticles and Disordered Media. *J Raman Spectrosc* **2020**, jrs.5815. https://doi.org/10.1002/jrs.5815.
(23) Stehlik, S.; Varga, M.; Ledinsky, M.; Miliaieva, D.; Kozak, H.; Skakalova, V.; Mangler, C.; Pennycook, T. J.; Meyer, J. C.; Kromka, A.; Rezek, B. High-Yield Fabrication and Properties of 1.4 Nm Nanodiamonds with Narrow Size Distribution. *Scientific Reports* **2016**, *6* (1). https://doi.org/10.1038/srep38419.
(24) Stehlik, S.; Varga, M.; Stenclova, P.; Ondic, L.; Ledinsky, M.; Pangrac, J.; Vanek, O.; Lipov, J.; Kromka, A.; Rezek, B. Ultrathin Nanocrystalline Diamond Films with Silicon Vacancy Color Centers via Seeding by 2 Nm Detonation Nanodiamonds. *ACS Applied Materials & Interfaces* **2017**, *9* (44), 38842–38853. https://doi.org/10.1021/acsami.7b14436.
(25) Rozbeský, D.; Kavan, D.; Chmelík, J.; Novák, P.; Vaněk, O.; Bezouška, K. High-Level Expression of Soluble Form of Mouse Natural Killer Cell Receptor NKR-P1C(B6) in Escherichia Coli. *Protein Expression and Purification* **2011**, *77* (2), 178–184. https://doi.org/10.1016/j.pep.2011.01.013.
(26) Schuck, P. Size-Distribution Analysis of Macromolecules by Sedimentation Velocity Ultracentrifugation and Lamm Equation Modeling. *Biophysical journal* **2000**, *78* (3), 1606–1619.
(27) Ilavsky, J. *Nika* : Software for Two-Dimensional Data Reduction. *J Appl Crystallogr* **2012**, *45* (2), 324–328. https://doi.org/10.1107/S0021889812004037.
(28) Ilavsky, J.; Jemian, P. R. *Irena* : Tool Suite for Modeling and Analysis of Small-Angle Scattering. *J Appl Crystallogr* **2009**, *42* (2), 347–353. https://doi.org/10.1107/S0021889809002222.
(29) Zhang, F.; Ilavsky, J.; Long, G. G.; Quintana, J. P. G.; Allen, A. J.; Jemian, P. R. Glassy Carbon as an Absolute Intensity Calibration Standard for Small-Angle Scattering. *Metall and Mat Trans A* **2010**, *41* (5), 1151–1158. https://doi.org/10.1007/s11661-009-9950-x.

(30) Kuznetsov, N. M.; Belousov, S. I.; Bakirov, A. V.; Chvalun, S. N.; Kamyshinsky, R. A.; Mikhutkin, A. A.; Vasiliev, A. L.; Tolstoy, P. M.; Mazur, A. S.; Eidelman, E. D.; Yudina, E. B.; Vul, A. Y. Unique Rheological Behavior of Detonation Nanodiamond Hydrosols: The Nature of Sol-Gel Transition. *Carbon* **2020**, *161*, 486–494. https://doi.org/10.1016/j.carbon.2020.01.054.

(31) Chang, S. L. Y.; Reineck, P.; Williams, D.; Bryant, G.; Opletal, G.; El-Demrdash, S. A.; Chiu, P.-L.; Ōsawa, E.; Barnard, A. S.; Dwyer, C. Dynamic Self-Assembly of Detonation Nanodiamond in Water. *Nanoscale* **2020**, *12* (9), 5363–5367. https://doi.org/10.1039/C9NR08984E.

(32) Kovářík, T.; Bělský, P.; Rieger, D.; Ilavsky, J.; Jandová, V.; Maas, M.; Šutta, P.; Pola, M.; Medlín, R. Particle Size Analysis and Characterization of Nanodiamond Dispersions in Water and Dimethylformamide by Various Scattering and Diffraction Methods. *J Nanopart Res* **2020**, *22* (2), 34. https://doi.org/10.1007/s11051-020-4755-3.

(33) Degen, T.; Sadki, M.; Bron, E.; König, U.; Nénert, G. The HighScore Suite. *Powder Diffr.* **2014**, *29* (S2), S13–S18. https://doi.org/10.1017/S0885715614000840.

(34) Mermoux, M.; Crisci, A.; Petit, T.; Girard, H. A.; Arnault, J.-C. Surface Modifications of Detonation Nanodiamonds Probed by Multiwavelength Raman Spectroscopy. *The Journal of Physical Chemistry C* **2014**, *118* (40), 23415–23425. https://doi.org/10.1021/jp507377z.

(35) Mermoux, M.; Marcus, B.; Abello, L.; Rosman, N.; Lucazeau, G. In Situ Raman Monitoring of the Growth of CVD Diamond Films. *J. Raman Spectrosc.* **2003**, *34* (7–8), 505–514. https://doi.org/10.1002/jrs.1012.

(36) Planken, K. L.; Cölfen, H. Analytical Ultracentrifugation of Colloids. *Nanoscale* **2010**, *2* (10), 1849. https://doi.org/10.1039/c0nr00215a.

(37) Cölfen, H.; Pauck, T. Determination of Particle Size Distributions with Angström Resolution. *Colloid & Polymer Science* **1997**, *275* (2), 175–180.

(38) Hammons, J. A.; Nielsen, M. H.; Bagge-Hansen, M.; Bastea, S.; Shaw, W. L.; Lee, J. R. I.; Ilavsky, J.; Sinclair, N.; Fezzaa, K.; Lauderbach, L. M.; Hodgin, R. L.; Orlikowski, D. A.; Fried, L. E.; Willey, T. M. Resolving Detonation Nanodiamond Size Evolution and Morphology at Sub-Microsecond Timescales during High-Explosive Detonations. *J. Phys. Chem. C* **2019**, *123* (31), 19153–19164. https://doi.org/10.1021/acs.jpcc.9b02692.

(39) Shenderova, O. A.; Vlasov, I. I.; Turner, S.; Van Tendeloo, G.; Orlinskii, S. B.; Shiryaev, A. A.; Khomich, A. A.; Sulyanov, S. N.; Jelezko, F.; Wrachtrup, J. Nitrogen Control in Nanodiamond Produced by Detonation Shock-Wave-Assisted Synthesis. *The Journal of Physical Chemistry C* **2011**, *115* (29), 14014–14024. https://doi.org/10.1021/jp202057q.

(40) Tomchuk, O. V.; Avdeev, M. V.; Dideikin, A. T.; Vul', A. Ya.; Aleksenskii, A. E.; Kirilenko, D. A.; Ivankov, O. I.; Soloviov, D. V.; Kuklin, A. I.; Garamus, V. M.; Kulvelis, Yu. V.; Aksenov, V. L.; Bulavin, L. A. Revealing the Structure of Composite Nanodiamond–Graphene Oxide Aqueous Dispersions by Small-Angle Scattering. *Diamond and Related Materials* **2020**, *103*, 107670. https://doi.org/10.1016/j.diamond.2019.107670.

(41) Hees, J.; Kriele, A.; Williams, O. A. Electrostatic Self-Assembly of Diamond Nanoparticles. *Chemical Physics Letters* **2011**, *509* (1–3), 12–15. https://doi.org/10.1016/j.cplett.2011.04.083.

(42) Yoshikawa, T.; Zuerbig, V.; Gao, F.; Hoffmann, R.; Nebel, C. E.; Ambacher, O.; Lebedev, V. Appropriate Salt Concentration of Nanodiamond Colloids for Electrostatic Self-Assembly Seeding of Monosized Individual Diamond Nanoparticles on Silicon Dioxide Surfaces. *Langmuir* **2015**, *31* (19), 5319–5325. https://doi.org/10.1021/acs.langmuir.5b01060.

(43) Peng, W.; Mahfouz, R.; Pan, J.; Hou, Y.; Beaujuge, P. M.; Bakr, O. M. Gram-Scale Fractionation of Nanodiamonds by Density Gradient Ultracentrifugation. *Nanoscale* **2013**, *5* (11), 5017. https://doi.org/10.1039/c3nr00990d.

(44) Korobov, M. V.; Avramenko, N. V.; Bogachev, A. G.; Rozhkova, N. N.; Osawa, E. Nanophase of Water in Nano-Diamond Gel. *Journal of Physical Chemistry C* **2007**, *111* (20), 7330–7334. https://doi.org/10.1021/jp0683420.
(45) Yur'ev, G. S.; Dolmatov, V. Yu. X-Ray Diffraction Study of Detonation Nanodiamonds. *Journal of Superhard Materials* **2010**, *32* (5), 311–328. https://doi.org/10.3103/S1063457610050035.
(46) Aleksenskii, A. E.; Baidakova, M. V.; Vul, A. Y.; Siklitskii, V. I. The Structure of Diamond Nanoclusters. *Physics of the solid state* **1999**, *41* (4), 668–671.
(47) Turner, S.; Shenderova, O.; Da Pieve, F.; Lu, Y.; Yücelen, E.; Verbeeck, J.; Lamoen, D.; Van Tendeloo, G. Aberration-Corrected Microscopy and Spectroscopy Analysis of Pristine, Nitrogen Containing Detonation Nanodiamond: Microscopy and Spectroscopy Analysis of Pristine, Nitrogen Containing DND. *physica status solidi (a)* **2013**, *210* (10), 1976–1984. https://doi.org/10.1002/pssa.201300315.
(48) Koniakhin, S. V.; Besedina, N. A.; Kirilenko, D. A.; Shvidchenko, A. V.; Eidelman, E. D. Ultracentrifugation for Ultrafine Nanodiamond Fractionation. *Superlattices and Microstructures* **2018**, *113*, 204–212. https://doi.org/10.1016/j.spmi.2017.10.039.
(49) Schmidlin, L.; Pichot, V.; Josset, S.; Pawlak, R.; Glatzel, T.; Kawai, S.; Meyer, E.; Spitzer, D. Two-Dimensional Nanodiamond Monolayers Deposited by Combined Ultracentrifugation and Electrophoresis Techniques. *Applied Physics Letters* **2012**, *101* (25), 253111. https://doi.org/10.1063/1.4772983.
(50) Usoltseva et al. - 2018 - Absorption Spectra of Nanodiamond Aqueous Dispersi.Pdf.
(51) Jirásek, V.; Stehlík, Š.; Štenclová, P.; Artemenko, A.; Rezek, B.; Kromka, A. Hydroxylation and Self-Assembly of Colloidal Hydrogenated Nanodiamonds by Aqueous Oxygen Radicals from Atmospheric Pressure Plasma Jet. *RSC Adv.* **2018**, *8* (66), 37681–37692. https://doi.org/10.1039/C8RA07873D.
(52) Artemenko, A.; Kozak, H.; Biederman, H.; Choukourov, A.; Kromka, A. Amination of NCD Films for Possible Application in Biosensing: Amination of NCD Films for Possible Application in Biosensing. *Plasma Processes and Polymers* **2015**, *12* (4), 336–346. https://doi.org/10.1002/ppap.201400151.
(53) Petit, T.; Arnault, J.-C.; Girard, H. A.; Sennour, M.; Bergonzo, P. Early Stages of Surface Graphitization on Nanodiamond Probed by X-Ray Photoelectron Spectroscopy. *Physical Review B* **2011**, *84* (23). https://doi.org/10.1103/PhysRevB.84.233407.
(54) Kusunoki, I.; Sakai, M.; Igari, Y.; Ishidzuka, S.; Takami, T.; Takaoka, T.; Nishitani-Gamo, M.; Ando, T. XPS Study of Nitridation of Diamond and Graphite with a Nitrogen Ion Beam. *Surface Science* **2001**, *492* (3), 315–328. https://doi.org/10.1016/S0039-6028(01)01430-3.
(55) Johansson, Å.; Stafström, S. A Δ-Self-Consistent-Field Study of the Nitrogen 1s Binding Energies in Carbon Nitrides. *The Journal of Chemical Physics* **1999**, *111* (7), 3203–3208. https://doi.org/10.1063/1.479662.
(56) Hellgren, N.; Haasch, R. T.; Schmidt, S.; Hultman, L.; Petrov, I. Interpretation of X-Ray Photoelectron Spectra of Carbon-Nitride Thin Films: New Insights from in Situ XPS. *Carbon* **2016**, *108*, 242–252. https://doi.org/10.1016/j.carbon.2016.07.017.
(57) Petit, T.; Puskar, L. FTIR Spectroscopy of Nanodiamonds: Methods and Interpretation. *Diamond and Related Materials* **2018**, *89*, 52–66. https://doi.org/10.1016/j.diamond.2018.08.005.
(58) Wolcott, A.; Schiros, T.; Trusheim, M. E.; Chen, E. H.; Nordlund, D.; Diaz, R. E.; Gaathon, O.; Englund, D.; Owen, J. S. Surface Structure of Aerobically Oxidized Diamond Nanocrystals. *The Journal of Physical Chemistry C* **2014**, *118* (46), 26695–26702. https://doi.org/10.1021/jp506992c.
(59) Petit, T.; Puskar, L.; Dolenko, T.; Choudhury, S.; Ritter, E.; Burikov, S.; Laptinskiy, K.; Brzustowski, Q.; Schade, U.; Yuzawa, H.; Nagasaka, M.; Kosugi, N.; Kurzyp, M.; Venerosy, A.; Girard, H.; Arnault, J.-C.; Osawa, E.; Nunn, N.; Shenderova, O.; Aziz, E. F. Unusual Water Hydrogen Bond

Network around Hydrogenated Nanodiamonds. *The Journal of Physical Chemistry C* **2017**, *121* (9), 5185–5194. https://doi.org/10.1021/acs.jpcc.7b00721.
(60) Jiang, T.; Xu, K.; Ji, S. FTIR Studies on the Spectral Changes of the Surface Functional Groups of Ultradispersed Diamond Powder Synthesized by Explosive Detonation after Treatment in Hydrogen, Nitrogen, Methane and Air at Different Temperatures. *Journal of the Chemical Society, Faraday Transactions* **1996**, *92* (18), 3401. https://doi.org/10.1039/ft9969203401.
(61) Ando, T.; Ishii, M.; Kamo, M.; Sato, Y. Thermal Hydrogenation of Diamond Surfaces Studied by Diffuse Reflectance Fourier-Transform Infrared, Temperature-Programmed Desorption and Laser Raman Spectroscopy. *Journal of the Chemical Society, Faraday Transactions* **1993**, *89* (11), 1783. https://doi.org/10.1039/ft9938901783.
(62) Lawson, S. C.; Fisher, D.; Hunt, D. C.; Newton, M. E. On the Existence of Positively Charged Single-Substitutional Nitrogen in Diamond. *J. Phys.: Condens. Matter* **1998**, *10* (27), 6171–6180. https://doi.org/10.1088/0953-8984/10/27/016.
(63) Titus, E.; Ali, N.; Cabral, G.; Madaleno, J. C.; Neto, V. F.; Gracio, J.; Ramesh Babu, P.; Sikder, A. K.; Okpalugo, T. I.; Misra, D. S. Nitrogen and Hydrogen Related Infrared Absorption in CVD Diamond Films. *Thin Solid Films* **2006**, *515* (1), 201–206. https://doi.org/10.1016/j.tsf.2005.12.062.
(64) Pichot, V.; Stephan, O.; Comet, M.; Fousson, E.; Mory, J.; March, K.; Spitzer, D. High Nitrogen Doping of Detonation Nanodiamonds. *The Journal of Physical Chemistry C* **2010**, *114* (22), 10082–10087.
(65) Stehlik, S.; Henych, J.; Stenclova, P.; Kral, R.; Zemenova, P.; Pangrac, J.; Vanek, O.; Kromka, A.; Rezek, B. Size and Nitrogen Inhomogeneity in Detonation and Laser Synthesized Primary Nanodiamond Particles Revealed via Salt-Assisted Deaggregation. *Carbon* **2021**, *171*, 230–239. https://doi.org/10.1016/j.carbon.2020.09.026.
(66) Matunová, P.; Jirásek, V.; Rezek, B. Structural and Electronic Properties of Oxidized and Amorphous Nanodiamond Surfaces with Covalently Grafted Polypyrrole. *Phys. Status Solidi B* **2019**, *256* (11), 1900176. https://doi.org/10.1002/pssb.201900176.
(67) Hassan, M. M.; Larsson, K. Effect of Surface Termination on Diamond (100) Surface Electrochemistry. *The Journal of Physical Chemistry C* **2014**, *118* (40), 22995–23002. https://doi.org/10.1021/jp500685q.
(68) Bosak, A.; Krisch, M. Phonon Density of States Probed by Inelastic X-Ray Scattering. *Physical Review B* **2005**, *72* (22). https://doi.org/10.1103/PhysRevB.72.224305.
(69) Shuker, R.; Gammon, R. W. Raman-Scattering Selection-Rule Breaking and the Density of States in Amorphous Materials. *Phys. Rev. Lett.* **1970**, *25* (4), 222–225. https://doi.org/10.1103/PhysRevLett.25.222.
(70) Ferrari, A. C.; Robertson, J. Raman Spectroscopy of Amorphous, Nanostructured, Diamond-like Carbon, and Nanodiamond. *Philosophical Transactions of the Royal Society A: Mathematical, Physical and Engineering Sciences* **2004**, *362* (1824), 2477–2512. https://doi.org/10.1098/rsta.2004.1452.
(71) Osswald, S.; Yushin, G.; Mochalin, V.; Kucheyev, S. O.; Gogotsi, Y. Control of Sp^2/Sp^3 Carbon Ratio and Surface Chemistry of Nanodiamond Powders by Selective Oxidation in Air. *Journal of the American Chemical Society* **2006**, *128* (35), 11635–11642. https://doi.org/10.1021/ja063303n.
(72) Matassa, R.; Orlanducci, S.; Reina, G.; Cassani, M. C.; Passeri, D.; Terranova, M. L.; Rossi, M. Structural and Morphological Peculiarities of Hybrid Au/Nanodiamond Engineered Nanostructures. *Scientific Reports* **2016**, *6* (1). https://doi.org/10.1038/srep31163.
(73) Korepanov, V. I.; Hamaguchi, H.; Osawa, E.; Ermolenkov, V.; Lednev, I. K.; Etzold, B. J. M.; Levinson, O.; Zousman, B.; Epperla, C. P.; Chang, H.-C. Carbon Structure in Nanodiamonds Elucidated from Raman Spectroscopy. *Carbon* **2017**, *121*, 322–329. https://doi.org/10.1016/j.carbon.2017.06.012.

(74) Obraztsova, E. D.; Korotushenko, K.; Pimenov, S. M.; Loubnin, N.; Inst, G.; Acad, R. RAMAN AND PHOTOLUMINESCENCE INVESTIGATIONS OF NANOGRAINED DIAMOND FILMS. 4.
(75) Filik, J.; Harvey, J. N.; Allan, N. L.; May, P. W.; Dahl, J. E. P.; Liu, S.; Carlson, R. M. K. Raman Spectroscopy of Nanocrystalline Diamond: An *Ab Initio* Approach. *Physical Review B* **2006**, *74* (3). https://doi.org/10.1103/PhysRevB.74.035423.
(76) Kaviani, M.; Deák, P.; Aradi, B.; Köhler, T.; Frauenheim, T. How Small Nanodiamonds Can Be? MD Study of the Stability against Graphitization. *Diamond and Related Materials* **2013**, *33*, 78–84. https://doi.org/10.1016/j.diamond.2013.01.002.
(77) Chang, S. L. Y.; Dwyer, C.; Ōsawa, E.; Barnard, A. S. Size Dependent Surface Reconstruction in Detonation Nanodiamonds. *Nanoscale Horizons* **2018**, *3* (2), 213–217. https://doi.org/10.1039/C7NH00125H.
(78) Shenderova, O. A.; McGuire, G. E. Science and Engineering of Nanodiamond Particle Surfaces for Biological Applications (Review). *Biointerphases* **2015**, *10* (3), 030802. https://doi.org/10.1116/1.4927679.
(79) Raty, J.-Y.; Galli, G.; Bostedt, C.; van Buuren, T.; Terminello, L. Quantum Confinement and Fullerenelike Surface Reconstructions in Nanodiamonds. *Physical Review Letters* **2003**, *90* (3). https://doi.org/10.1103/PhysRevLett.90.037401.
(80) Fang, X.; Mao, J.; Levin, E. M.; Schmidt-Rohr, K. Nonaromatic Core−Shell Structure of Nanodiamond from Solid-State NMR Spectroscopy. *Journal of the American Chemical Society* **2009**, *131* (4), 1426–1435. https://doi.org/10.1021/ja8054063.
(81) Palosz, B.; Pantea, C.; Grzanka, E.; Stelmakh, S.; Proffen, Th.; Zerda, T. W.; Palosz, W. Investigation of Relaxation of Nanodiamond Surface in Real and Reciprocal Spaces. *Diamond and Related Materials* **2006**, *15* (11–12), 1813–1817. https://doi.org/10.1016/j.diamond.2006.09.001.
(82) Beck, R. A.; Petrone, A.; Kasper, J. M.; Crane, M. J.; Pauzauskie, P. J.; Li, X. Effect of Surface Passivation on Nanodiamond Crystallinity. *The Journal of Physical Chemistry C* **2018**, *122* (15), 8573–8580. https://doi.org/10.1021/acs.jpcc.8b00354.
(83) Paillard, V.; Puech, P.; Laguna, M. A.; Carles, R.; Kohn, B.; Huisken, F. Improved One-Phonon Confinement Model for an Accurate Size Determination of Silicon Nanocrystals. *Journal of Applied Physics* **1999**, *86* (4), 1921–1924. https://doi.org/10.1063/1.370988.
(84) Ledinský, M.; Vetushka, A.; Stuchlík, J.; Mates, T.; Fejfar, A.; Kočka, J.; Štěpánek, J. Crystallinity of the Mixed Phase Silicon Thin Films by Raman Spectroscopy. *Journal of Non-Crystalline Solids* **2008**, *354* (19–25), 2253–2257. https://doi.org/10.1016/j.jnoncrysol.2007.09.073.
(85) Richter, H.; Wang, Z. P.; Ley, L. THE ONE PHCNON RAMAN SPECTRUM IN MICROCRYSTALLINE SILICON. *39* (5), 5.
(86) Campbell, I. H.; Fauchet, P. M. The Effects of Microcrystal Size and Shape on the One Phonon Raman Spectra of Crystalline Semiconductors. *Solid State Communications* **1986**, *58* (10), 739–741. https://doi.org/10.1016/0038-1098(86)90513-2.
(87) Pavone, P.; Karch, K.; Schütt, O.; Strauch, D.; Windl, W.; Giannozzi, P.; Baroni, S. *Ab Initio* Lattice Dynamics of Diamond. *Phys. Rev. B* **1993**, *48* (5), 3156–3163. https://doi.org/10.1103/PhysRevB.48.3156.
(88) Windl, W.; Pavone, P.; Karch, K.; Schütt, O.; Strauch, D.; Giannozzi, P.; Baroni, S. Second-Order Raman Spectra of Diamond from *Ab Initio* Phonon Calculations. *Phys. Rev. B* **1993**, *48* (5), 3164–3170. https://doi.org/10.1103/PhysRevB.48.3164.
(89) Kulda, J.; Kainzmaier, H.; Strauch, D.; Dorner, B.; Lorenzen, M.; Krisch, M. Overbending of the Longitudinal Optical Phonon Branch in Diamond as Evidenced by Inelastic Neutron and X-Ray Scattering. *Phys. Rev. B* **2002**, *66* (24), 241202. https://doi.org/10.1103/PhysRevB.66.241202.

(90) Saviot, L.; Champagnon, B.; Duval, E.; Kudriavtsev, I. A.; Ekimov, A. I. Size Dependence of Acoustic and Optical Vibrational Modes of CdSe Nanocrystals in Glasses. *Journal of Non-Crystalline Solids* **1996**, *197* (2–3), 238–246. https://doi.org/10.1016/0022-3093(96)00164-0.
(91) Portales, H.; Saviot, L.; Duval, E.; Fujii, M.; Hayashi, S.; Del Fatti, N.; Vallée, F. Resonant Raman Scattering by Breathing Modes of Metal Nanoparticles. *The Journal of Chemical Physics* **2001**, *115* (8), 3444–3447. https://doi.org/10.1063/1.1396817.
(92) Montagna, M.; Dusi, R. Raman Scattering from Small Spherical Particles. *Phys. Rev. B* **1995**, *52* (14), 10080–10089. https://doi.org/10.1103/PhysRevB.52.10080.
(93) Duval, E. Far-Infrared and Raman Vibrational Transitions of a Solid Sphere: Selection Rules. *Phys. Rev. B* **1992**, *46* (9), 5795–5797. https://doi.org/10.1103/PhysRevB.46.5795.
(94) Https://Saviot.Cnrs.Fr/Index.Html.
(95) Anastassakis, E.; Siakavellas, M. Elastic Properties of Textured Diamond and Silicon. *Journal of Applied Physics* **2001**, *90* (1), 144–152. https://doi.org/10.1063/1.1332096.
(96) Werner, M.; Hein, S.; Obermeier, E. Elastic Properties of Thin Polycrystalline Diamond Films. *Diamond and Related Materials* **1993**, *2* (5–7), 939–942. https://doi.org/10.1016/0925-9635(93)90254-Y.

TOC graphic: